Supporting Information

Spin-Chemical Effects on Intramolecular Photoinduced Charge Transfer Reactions in Bisphenanthroline Copper(I)-Viologen Dyad Assemblies

Megan S. Lazorski,*[a][α][†] Igor Schapiro,[b][β][†] Ross S. Gaddie,[a] Ammon P. Lehnig,[a] Mihail Atanasov,[b] Frank Neese,*[b] Ulrich E. Steiner,*[c] and C. Michael Elliott[a][‡]

[a]Department of Chemistry, Colorado State University, Fort Collins, CO 80523. [b]Max Planck Institute for Chemical Energy Conversion, D-45470 Mülheim an der Ruhr, Germany.
[c]Department of Chemistry, University of Konstanz, Universitätsstraße 14, Konstanz, 78457, Germany

Contents

A. Ligand and Copper Complex Synthesis

Other than the following exceptions, all starting materials and solvents were solvent grade or better, obtained from commercial sources, and used without further purification. The 1,2-difluorobenzene (dfb) was obtained from Oakwood Products, Inc. and run through a column of neutral, activated Al_2O_3 before use. The hydrazine sulfate used in the synthesis of Me-Diol (see **Scheme S1**) was recrystallized from water and dried thoroughly in the vacuum oven before use. Tetrakis(acetonitrile)copper(I) tetrafluoroborate ($[Cu(ACN)_4]^+BF_4^-$) was recrystallized from acetonitrile before use and stored in a dessicator. UltimAr acetonitrile (ACN) was obtained from MACRON Chemicals. DriSolv dimethylformamide (DMF), OmniSolv dichloromethane (DCM), and OmniSolv methanol (MeOH) were obtained from EMD Chemicals. Potassium tetrakis(pentafluorophenyl)borate was obtained from Boulder Scientific. Tris(bipyridine)ruthenium(II) hexafluorophosphate ($[Ru(bpy)_3]^{2+}(PF_6^-)_2$) was synthesized as published previously.[1] Solutions of MeOH in dfb are reported as v/v percentage. Literature methods were used to prepare the 2,9-di(R=methyl or phenyl)-1,10-phenanthroline-5,6-diol (R-Diol) from **Scheme S1**, as well as its precursor the 2,9-di(R=methyl or phenyl)-1,10-phenanthroline-5,6-dione (R-Dione).[2–6] In addition to structural verification by ^{1}H NMR, the purity of intermediates and final ligands was also typically verified by silica gel TLC. In the

case of compounds which are charged, the elution solvent was 5:4:1 acetonitrile:water:KNO$_3$ *(sat. aq)*. Static UV-Visible spectra were obtained using air-tight cells (vide infra) and an Agilent 8453 diode array spectrometer.
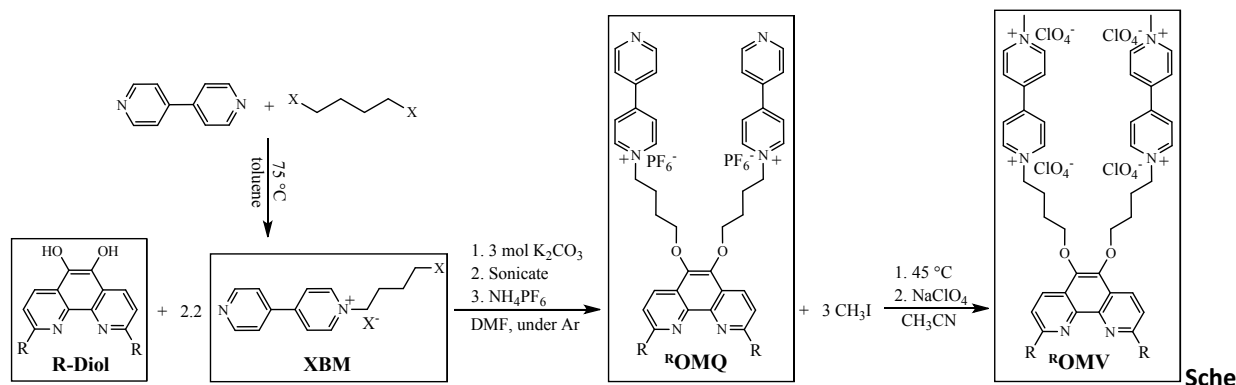
me S1 A typical synthesis of the ^{R}OMV acceptor ligand (X=I or Br; R= Me or Ph; e.g. methyl or phenyl, See text for details).

Halobutyl bipyridinium salts: *1-(4-iodobutyl)-[4,4'-bipyridin]-1-ium Iodide* (IBM) *or 1-(4-bromobutyl)-[4,4'-bipyridin]-1-ium Bromide* (BBM): To a solution of 4,4'-bipyridine in toluene, 1,4-diiodobutane or 1,4-dibromobutane (1:1 molar ratio) was added. The solution was heated at 75 °C overnight in a stoppered flask. The resulting red/orange precipitate was collected via filteration, then washed thoroughly with absolute ethanol. The ethanol rinseates were combined and the solvent was removed in vacuo affording a yellow/orange solid, which was recrystallized from ethanol to give the purified product. ^{1}H NMR of IBM (400 MHz, CD$_3$CN, δ): 8.85 (t, 4H, Ar-pyridine), 8.34 (d, 2H, Ar-pyridine), 7.80 (d, 2H, Ar-pyridine), 4.62 (t, 2H, -N-CH$_2$), 3.29 (t, 2H, I-CH$_2$), 2.11 (m, 2H, I-CH$_2$-C*H*$_2$), 1.89 (m, 2H, -N-CH$_2$-C*H*$_2$). ^{1}H NMR of BBM (400 MHz, D$_2$O, δ): 8.83 (d, 2H, Ar-pyridine),8.63 (d, 2H, Ar-pyridine), 8.27 (d, 2H, Ar-pyridine), 7.77 (d, 2H, Ar-pyridine), 4.56 (t, 2H, -N-CH$_2$), 3.40 (t, 2H, Br-CH$_2$), 2.09 (m, 2H, N-CH$_2$-C*H*$_2$), 1.81 (m, 2H, Br-CH$_2$-C*H*$_2$) .

^{Me}**OMQ:** *1,1''-(((2,9-dimethyl-1,10-phenanthroline-5,6-diyl)bis(oxy))bis(butane-4,1-diyl))bis([4,4'-bipyridin]-1-ium) Hexafluorophosphate*: To a 100 mL round bottomed flask was added 0.510 g potassium carbonate, 0.295 g Me-Diol, and 1.20 g of IBM (3:1: 2.1 mol), each of which was dried in the vacuum oven for at least 12 hours before use. The flask was purged with Ar and 10 mL of dry, degassed DMF was added via syringe. The flask containing the reaction mixture was sonicated in an ice bath, which slowly warmed

to 45 °C due to the sonication, and sonicated at 45 °C for 12 hours. The DMF was removed in vacuo and the resulting viscous brown oil was sonicated in excess water. The water rinseates were filtered through Celite to remove a black, tarry byproduct.   The aqueous filtrate was collected, reduced in volume, precipitated by adding solid NH_4PF_6, and the resulting precipitate was collected via centrifugation. The crude product was purified by dissolving in hot MeOH, and filtering through celite. As the filtrate cooled, the product precipitated from solution as a light beige solid which was collected by filtration. ^{1}H NMR (400 MHz, CD_3CN, δ): 8.86 (dd, 4H, Ar-pyridine), 8.74 (d, 4H, Ar-pyridine), 8.41 (d, 2H, 4,7-phen), 8.27 (d, 4H, Ar-pyridine), 7.77 (dd, 4H, Ar-pyridine), 7.54 (d, 2H, 3,8-phen), 4.62 (t, 4H, N-CH_2), 4.25 (t, 4H, O-CH_2), 2.76 (s, 6H, CH_3), 2.25 (m, 4H, -O-CH_2-CH_2), 1.89 (m, 4H, -N-CH_2-CH_2). HRMS: ESI/APCI-TOF *m/z* (relative intensity): [(M-PF_6)+H]$^+$ calcd for $C_{42}H_{42}F_6N_6O_2P$, 807.3006; found 807.3009.

^{Me}OMV: *1',1'''-(((2,9-dimethyl-1,10-phenanthroline-5,6-diyl)bis(oxy))bis(butane-4,1-diyl))bis(1-methyl-[4,4'bipyridine]-1,1'-diium) Perchlorate*: To a cold solution of 0.10 g of ^{Me}OMQ in 2 mL of ACN was added 20 μL of methyl iodide (1:3 mol). A Teflon lined vial cap was placed on the reaction vial which was heated to 45 °C for 24 hrs. The resulting red was filtered, rinsed with acetonitrile, and subsequently rinsed with MeOH. The MeOH rinsate was collected and 1 mL of $NaClO_4$ $_{(sat'd)}$ in MeOH was added. The beige precipitate was collected via filtration and rinsed with 15 mL hot MeOH. To the hot MeOH rinsate was added 5 mL of isopropanol and the solution was quickly cooled to -17 °C. The product was collected as light beige solids. ^{1}H NMR (400 MHz, CD_3CN, δ): 8.96 (d, 4H, Ar-pyridine), 8.86 (d, 4H, Ar-pyridine), 8.48 (d, 2H, 4,7-phen), 8.40 (d, 8H, Ar-pyridine), 7.60 (d, 2H, 3,8-phen), 4.74 (t, 4H, N-CH_2), 4.41 (s, 6H, CH_3-pyridine), 4.28 (t, 4H, O-CH_2), 2.80 (s, 6H, 2,9-phen-CH_3), 2.32 (m, 4H, -O-CH_2-CH_2), 1.97 (m, 4H, -N-CH_2-CH_2).   HRMS: ESI/APCI *m/z* (relative intensity): [M-$ClO_4$$^-$]$^+$ calcd for $C_{44}H_{48}Cl_3N_6O_{14}$, 991.2271; found 991.2267.

^{Ph}OMQ: *1,1''-(((2,9-diphenyl-1,10-phenanthroline-5,6-diyl)bis(oxy))bis(butane-4,1-diyl))bis([4,4'-bipyridin]-1-ium) Perchlorate*: In a typical reaction, in an inert atmosphere box 50 mg of P-Dione was added to a 20 mL scintillation vial along with 6.4 mg of sodium metal (2 eq.) and 5 mL of anhydrous DMF,

which was stirred overnight resulting in a dark red solution. Ammonium nitrate (19.9 mg, 1.8 eq.), which had been previously dried at 80 °C in a vacuum oven, was added to the solution. The resulting diol solution was amber in color and used without isolation. Anhydrous cesium carbonate (135.0 mg, 3.0 eq.) and solid BBM (128.4 mg. 2.5 eq.) were added to the diol solution and the reaction was stirred for 24 hours under inert atmosphere. On the benchtop, a few drops of H_2O and a small piece of dry ice were added to the reaction to neutralize any excess Cs_2CO_3. After all of the solid CO_2 had sublimed, the solvent was removed under vacuum to yield a dark brown tar.

The residue above was extracted thoroughly with MeOH, the MeOH extracts were combined, and a concentrated methanolic solution of $NaClO_4$ was added dropwise while swirling to afford a grey/tan flocculent precipitate. The solution was centrifuged to isolate the solid. The isolated solids were re-suspended in pure MeOH and re-centrifuged. The product was dried in vacuo, dissolved in ACN (ca. 10 mL) and transferred to a scintillation vial. Approximately 50 mg of activated silica gel (Aldrich 70-230 mesh) was added to this solution and the vial tightly capped. The vial was then placed on its side on a rocker table and roll back and forth overnight. The light-yellow solution was decanted from the silica gel into a round bottom flask and the silica washed with several ca. 1 mL portions of ACN, which were combined with product solution in the round bottom flask. Approximately 50 mg of $NaClO_{4(s)}$ was added to the flask and the ACN removed in vacuo to yield a light yellow/tan residue. Approximately 10 mL of H_2O was added to the flask and product was collected by vacuum filtration and washed with several portions of H_2O. ^{1}H NMR (400 MHz, CD_3CN, δ): 8.81 (d, 4H, Ar-pyridine), 8.73 (d, 4H, Ar-pyridine), 8.63 (d, 2H, 4,7-phen), 8.44 (d, 4H, 2,9-phen-o-Ph), 8.25 (d, 2H, 3,8-phen), 8.23 (d, 4H, Ar-pyridine), 7.73 (d, 4H, Ar-pyridine), 7.64 (t, 4H, 2,9-phen-m-Ph), 7.56 (t, 2H, 2,9-phen-p-Ph), 4.62 (t, 4H, N-CH$_2$), 4.35 (t, 4H, O-CH$_2$), 2.27 (m, 4H, O-CH$_2$-C*H*$_2$), 1.94 (m, 4H, N-CH$_2$-C*H*$_2$)

[Ph]**OMV:**   *1',1'''-(((2,9-diphenyl-1,10-phenanthroline-5,6-diyl)bis(oxy))bis(butane-4,1-diyl))bis(1-methyl-[4,4'bipyridine]-1,1'-diium) Perchlorate*: The same procedure was followed as for converting the [Me]OMQ to [Me]OMV with the following exceptions: after alkylation, conversion to the perchlorate salt was accomplished by dissolving the mixed I⁻/ClO₄⁻ product [Ph]OMV in a mixture of H_2O/MeOH/acetonitrile and

adding excess $NaClO_{4(s)}$ followed by removal of solvent by rotary evaporation. Water was then added to the flask to suspend the product, which was isolated by vacuum filtration. ^1H NMR (400 MHz, CD_3CN, δ): 8.83 (d, 4H, Ar-pyridine), 8.76 (d, 4H, Ar-pyridine), 8.64 (d, 2H, 4,7-phen), 8.42 (d, 4H, Ar-pyridine), 8.32 (d, 4H, 2,9-phen--phenyl), 8.27(d, 2H, 3,8-phen-phenyl), 8.23 (d, 4H, Ar-pyridine), 7.67 (t, 4H, 2,9-phen-phenyl), 7.60 (t, 2H, 2,9-phen-phenyl), 4.69 (t, 4H, N-CH_2), 4.38 (t, 4H, O-CH_2), 4.35 (s, 6H, N-CH_3), 2.29 (m, 4H, O-CH_2-CH_2), 1.94 (m, 4H, N-CH_2-CH_2).

[Cu(I)(^{R}phen(OMV)$_2$$^{4+}$)$_2$]$^{9+}$ (TPFB$^-$)$_9$: *Di-(1',1'''-(((2,9-dimethyl-1,10-phenanthroline-5,6-diyl)bis(oxy))bis(butane-4,1-diyl))bis(1-methyl-[4,4'bipyridine]-1,1'-diium))copper(I) Tetrakis(pentafluorophenyl) borate(^{Me}C$^+$A$_4$$^{8+}$) or Di-(1',1'''-(((2,9-diphenyl-1,10-phenanthroline-5,6-diyl)bis(oxy))bis(butane-4,1-diyl))bis(1-methyl-[4,4'bipyridine]-1,1'-diium))copper(I) Tetrakis(pentafluorophenyl) borate (^{Ph}C$^+$A$_4$$^{8+}$):* A typical preparation of a stock solution of the diad complexes for spectral measurement (TA or UV-vis) is as follows: To a vial containing 1 mL of ACN (UltimAr) was added 0.0052 g (1.5 molar xs) potassium tetrakis(pentafluorophenyl)borate (TPFB$^-$), 109 µL of a 9.2 mM ^{R}OMV solution in ACN, and 157 µl of a 3.2 mM solution of [Cu(ACN)$_4$]$^+$BF$_4$$^-$ in ACN (2:1 molar ratio), in that order, after which the solvent was removed in vacuo. The complex was then brought into the inert atmosphere box and dissolved in 2.5 mL degassed dfb. ^1H NMR of [Cu(I)(^{Me}phen(OMV)$_2$$^{4+}$)$_2$]$^{9+}$ (TPFB$^-$)$_9$ (400 MHz, CD_3OD, δ): 9.28 (d, 4H, Ar-pyridine), 9.15 (d, 4H, Ar-pyridine), 8.69 (d, 2H, 4,7-phen), 8.65 (d, 4H, Ar-pyridine), 8.60 (d, 4H, Ar-pyridine), 7.73 (d, 2H, 3,8-phen), 4.88 (t, 4H, N-CH_2), 4.50 (s, 6H, CH_3-pyridine), 4.38 (t, 4H, O-CH_2), 2.45 (m, 4H, -O-CH_2-CH_2), 2.31 (s, 6H, 2,9-phen-CH_3), 2.11 (m, 4H, -N-CH_2-CH_2).

 Since Cu(I) complexes suffer from inherent lability, the complexes must self-assemble in solution through the method described above, precluding many standard methods of isolation, purification, and characterization. To address this, detailed titration experiments were performed via ^1H NMR, UV-vis and cyclic voltammetry (CV) to verify the purity and stoichiometric ratio of the complexes as assembled. A typical experiment would proceed as follows: two molar equivalents of the ^{R}OMV ligand was placed in an appropriate solvent (For ^1H NMR: typically CD_3CN/CD_2Cl_2 (1:1 v/v) or CD_3OD/CD_2Cl_2 (1:1 v/v); for UV-vis and CV typically CH_3CN, CH_3OH, or a mixture of CH_3CN or CH_3OH with CH_2Cl_2 or 1,2-difluorobenzene) and

a spectrum was recorded. After measuring the spectrum of the free ligand, a solution of $[Cu(CH_3CN)_4](X^-)$ (X^- = tetrafluoroborate (BF_4^-), perchlorate (ClO_4^-), hexafluorophosphate (PF_6^-), tetrakis[3,5-bis(trifluoromethyl)phenyl]borate (BARF$^-$), or tetrakis(pentafluorophenyl)borate (TPFB$^-$)) was incrementally added to the solution, in either 0.25 or 0.5 molar equivalent aliquots, and a spectrum was recorded after each addition. In all of these experiments, consistent, reproducible spectra were afforded. In the ^{1}H NMR experiments, differentiation of the mono- and di-substituted C-A dyads, $[Cu(^ROMV)(solvent)_2](X^-)$ and $[Cu(^ROMV)_2](X^-)$, was facile and reproducible enough to enable relative quantitation of each compound in solution within a few weight %, adding credence to the ^{1}H NMR assignments above. In the CV experiments, the obtained redox behavior of the ^ROMV was unaffected by coordination, as expected based on the distance of the acceptor moiety from the coordination sphere. However, coordination was verified by a copper stripping peak that emerges after the molar ratio exceeds 2:1 ($^R4OMV:Cu^+$), as is evident in **Figure S1** for the C-A dyad with ^{Me}OMV. If the monosubstituted solvento complex had formed, $[Cu(^ROMV)(solv)_2]^+(X^-)$, the stripping peak would not have been observed until the $^R4OMV:Cu^+$ ratio exceeded 1:1 stoichiometry. Additionally, the CV data was an excellent secondary confirmation of the sample purity due to the lack of any other redox signals on the µA scale over a wide potential range.
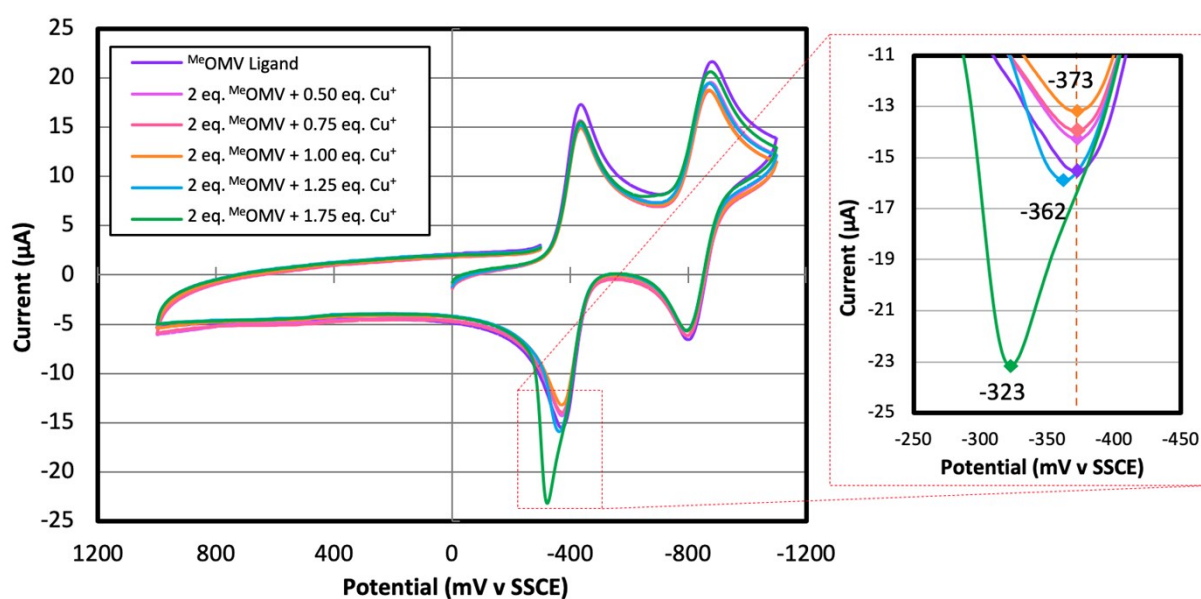

Figure S1. A representative CV titration experiment verifying the formation of pure 2:1 homoleptic complexes with the ^4OMV acceptor ligands. In this particular experiment, the electrolyte solution was 0.1 M tetrabutylammonium hexafluorophosphate (TBA$^+$(PF$_6^-$)) in optima acetonitrile (Working electrode: glassy

carbon, Auxiliary electrode: Pt coil, Scan rate : 50 mV/sec, Initial potential sweep: negative). Inset: A shift in the peak potential is evident after the [R]4OMV:Cu^{+} ratio exceeds 2:1 stoichiometry as the stripping peak emerges.

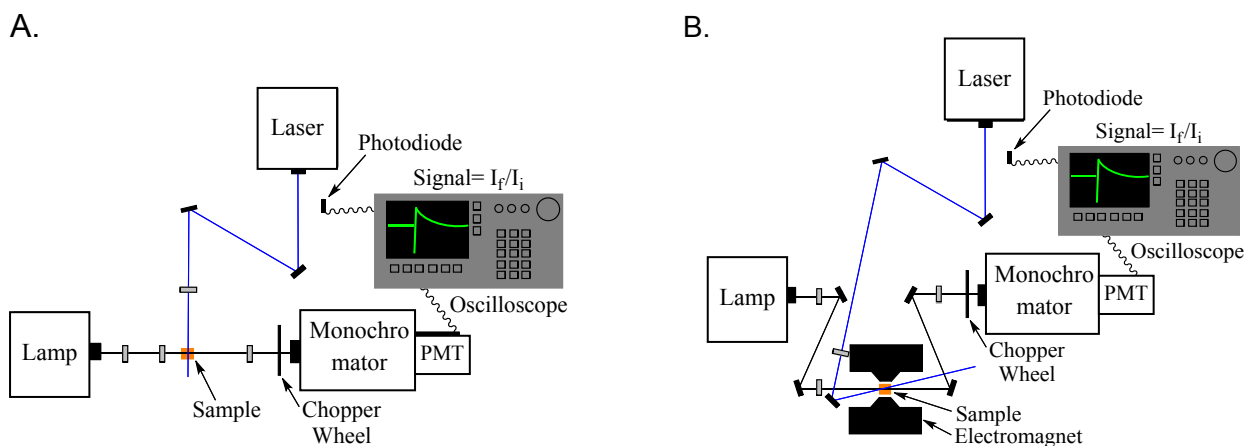## B. Optical Setup for Transient Absorption Spectroscopy

A.

B.

Figure S2 Schematic of the transient absorption laser set-up. A) Set-up used to determine CT/CS lifetime and transient absorption spectra in absence of magnetic field. B) Set-up used to for determining lifetime of CT/CS and initial intensities in a magnetic field.

Signal Processing

The signal was processed as follows when the decay times of transient signals would be affected by the time profile of the laser pulse. To correct for the finite duration of the pumping period, the observed signals were fit using either Origin 7.5 advanced fitting function or a nonlinear regression fitting function in the statistical computing software R[7] which fit a differential equation simulating the excitation and subsequent decay of CT state during and after each laser pulse.

Examples of the laser pulse profile measured by a Thorlabs DET210 high speed photodiode detector (rise/fall time 1 ns) are shown in **Figure S3**. They can be reproduced rather well by Gaussian profiles with FWHM of 4.0 ± 0.1 ns.
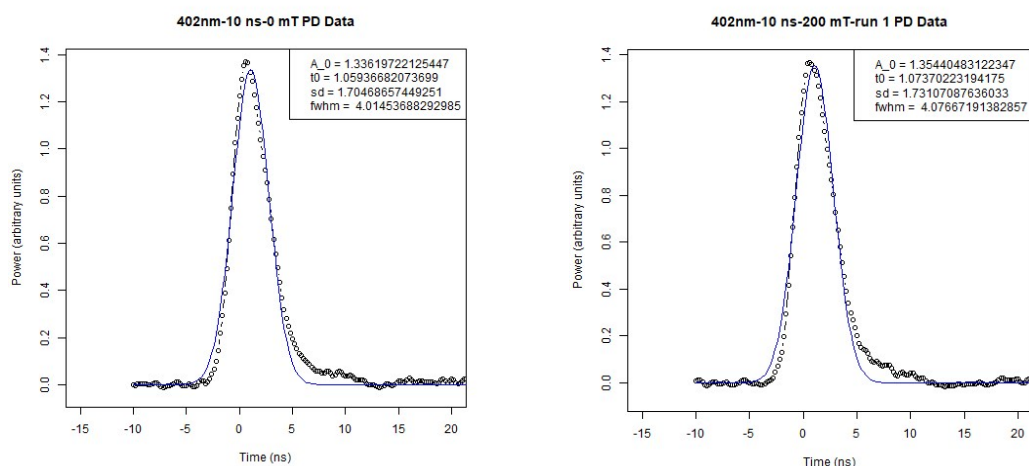
Figure S3 Laser time profiles measured with the photodiode and Gaussian fits.
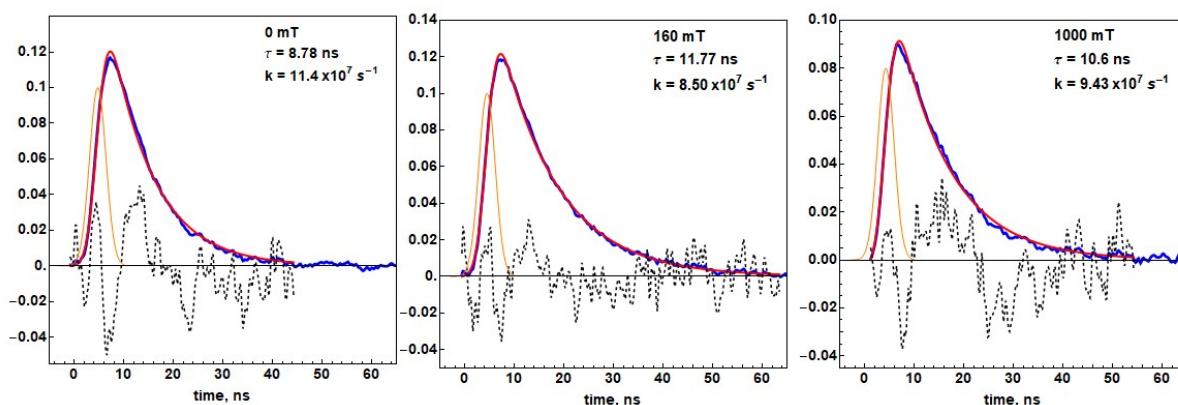

Figure S4 Detected signals at various fields (blue). Laser profile, represented by a Gaussian of 4.0 ns FWHM (orange), result of ODE-fit (red), residualx10 (dashed, black). The resulting decay times/rate constants of decay are given as insets.

The transient signals were measured with a Hamamatsu PMT R2496 (fast time response 0.6 ns). Examples of recorded signals and ODE fits are shown in **Figure S4**. In the fits, Gaussian time profiles of the laser pulse were used with adjustable width. The best fits were obtained with a FWHM value of 4.0 ns, which nicely fits the laser profile widths measured with the photodiode.

C. Solvent Effects on Initial Amplitude of $^{Me}C^{+}A_{4}^{8+}$

As the MeOH concentration increases, so does the initial amplitude of the TA signal for $^{Me}C^{+}A_{4}^{8+}$ (**Figure S5A**). However, there is a concomitant increase in the magnitude of the [Cu(I)P$_2$] MLCT band in the static absorption spectrum with the first several additions of MeOH to the cell(**Figure S5B**). This may be due to a change in the absorption coefficient, but, although no solids were visible in the initial solution, the increased absorbance, in this case, may at least partially be due

to the increased solubility of the complex when MeOH is present. This explanation is supported by the fact that there is also essentially no difference in the MLCT band shape in the presence and absence of MeOH in solution. Furthermore, a slight decrease in the initial amplitude of the CT absorbance for the highest MeOH concentration is consistent with the simple dilution of the $^{Me}C^+A_4^{8+}$ concentration with the added volume of MeOH (evident in both the static and TA spectra). The static absorbance at λ_{max} for 0% and 2% MeOH concentrations differ by ca. 30% whereas the maximum ΔA in the transient absorbance differs by approximately a factor of two. This difference is a result of the short lifetime for the CT state in the absence of MeOH (see discussion of the fitting approaches in the Experimental Section). When the MaxΔA values obtained from the ODE fits are compared for the 0 and 2% MeOH solutions, their values match the difference in the ground state absorbance (i.e., ca. 30%; cf. table inserts in **Figure S5B**). This can be seen more clearly from the values of MaxΔA normalized for the absorbance at λ_{max} presented in the last column of the table insert in **Figure S5B**. From these data, there is an apparent increase in the initial amount of CT formed per unit $^{Me}C^+A_4^{8+}$. There are several possible

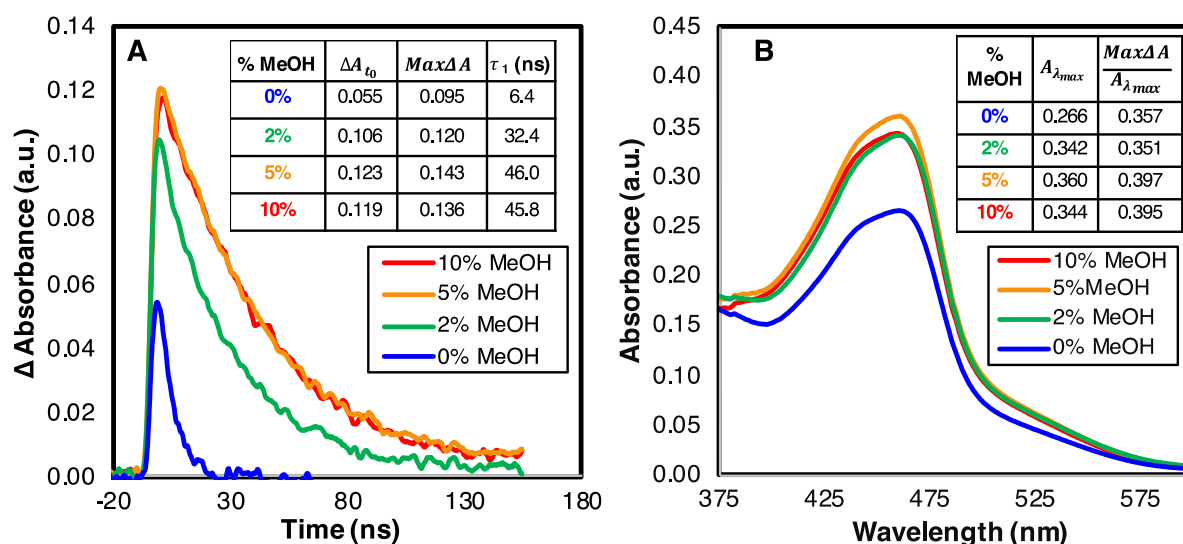Table inset in (A):

% MeOH	ΔA_{t_0}	$Max\Delta A$	τ_1 (ns)
0%	0.055	0.095	6.4
2%	0.106	0.120	32.4
5%	0.123	0.143	46.0
10%	0.119	0.136	45.8

Table inset in (B):

% MeOH	$A_{\lambda max}$	$\dfrac{Max\Delta A}{A_{\lambda max}}$
0%	0.266	0.357
2%	0.342	0.351
5%	0.360	0.397
10%	0.344	0.395

Figure S5 (A) The effect on the single-wavelength TA of $^{Me}C^+A_4^{8+}$ in dfb/X% MeOH at 396 nm (λ_{ex}=475 nm), and (B) static spectra as a function of %[MeOH]. The table inset in (A) provides the measured delta absorbance at t=0 (ΔA_{t0}), the calculated delta absorbance at t=0 using the ODE-fitting technique (MaxΔA), and the lifetime resulting from the ODE fit (τ_1). The table inset in (B) provides the total change in MaxΔA for comparison to the change in static absorbance with MeOH concentration. The data shown in (A) were obtained with a small (25 mT) applied magnetic field due to a logistical issue; however, the effect of a magnetic field on the CT lifetime is small at this field and are thus still accurate for zero field within a few percent.

causes for this change in initial amplitude. In sum, this effect is likely due to a combination of factors: increased solubility, longer τ_{CT}, and an approximately 10% increase in initial CT state formation as MeOH concentration increases from 0-5%.

D. Quantum Chemistry

Geometry optimization

In order to analyze the geometries of the intermediates along the reaction scheme (**Scheme S2**) we have performed geometry optimizations. All structures were minimized with tightened convergence criteria, without symmetry or any type of restraints. The ground state singlet minimum was obtained using the restricted while the doublet and triplet using the unrestricted B3LYP, respectively. Excited-states geometries were obtained using TD-DFT.[8] The ^{1}MLCT minimum for $[Cu(dmp)_2]^+$ and $[Cu(dpp)_2]^+$ was obtained by including four and five lowest roots, respectively, in the TD-DFT calculation. The choice was made because we found the fourth or the sixth root to be the spectroscopically active excited state for the corresponding complex at the Franck-Condon point. The analytic gradients were calculated for the second root in the optimization of the relaxed excited state minimum.
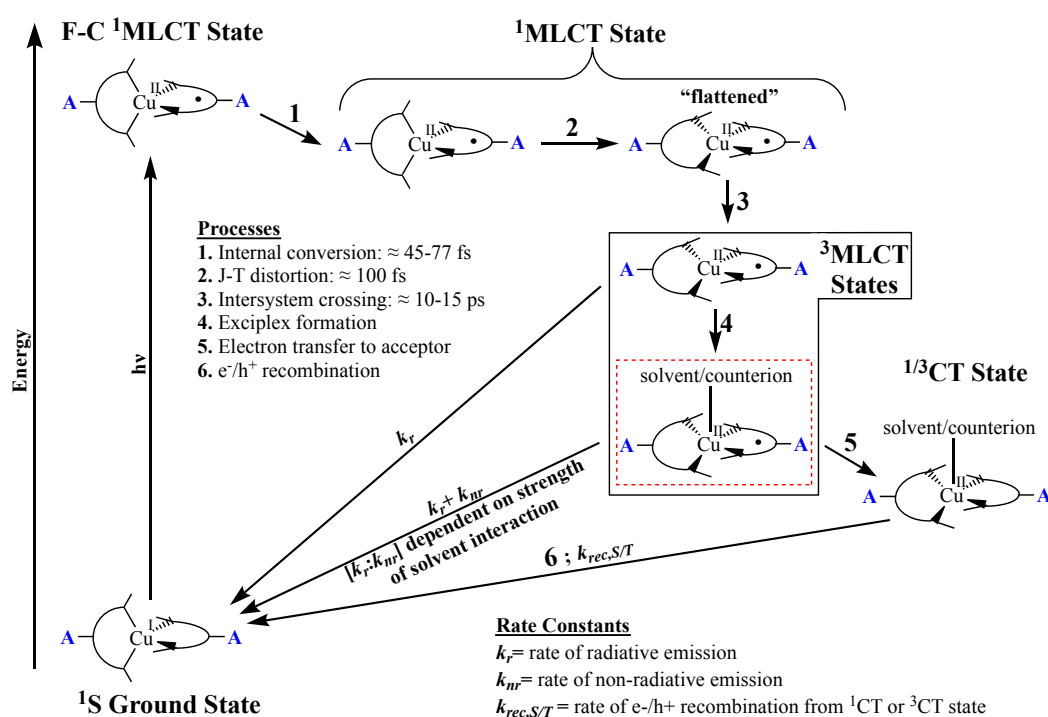
Scheme S2 Reaction path of the Cu(phen)$_2$-diad, modified from Refs 9 and 10.

Results of the geometry optimization

[Cu(dmp)$_2$]+

The optimized ground state geometry of [Cu(dmp)$_2$]$^+$ shows D$_{2d}$ symmetry with considerable distortion from tetrahedral geometry (**Figure S6**). The intraligand and interligand N-Cu-N bond angles are 82.4° and 124.5°, respectively. The dihedral angle between the two phen planes (ϑ_z) is 90° and all the Cu-N bonds are identical with 2.044 Å (**Table S1**). Upon excitation the S$_3$ state is populated, which is characterized by a promotion of one electron from the d$_{xz}$ and d$_{yz}$ orbitals to a linear combination of π*-orbitals of the ligand. Hence, this is a metal-to-ligand charge transfer (MLCT) state, which becomes apparent from the difference density in **Figure S7**. This transition is dipole allowed and has the highest oscillator strength (0.22) among the states within the visible range. The calculated vertical S$_0$-S$_3$ excitation energy of 2.6 eV (21050 cm^{-1} (475 nm)) is in good agreement with the one deduced from the experimental absorption band maximum at 22200 cm^{-1} (460 nm).[11]
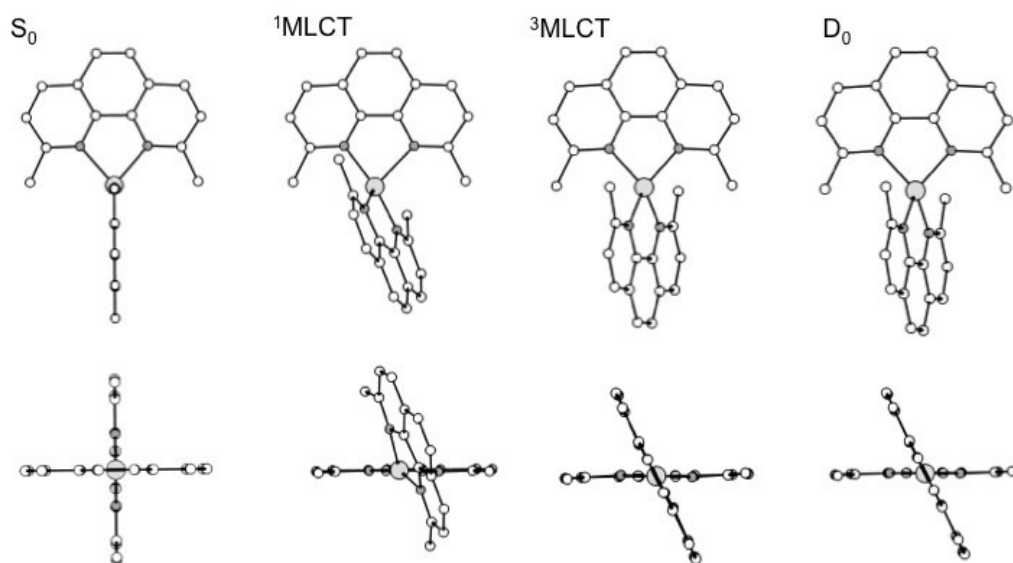

Figure S6 Geometries of the dmp model. From the left to the right the minimum of the ground state, the lowest ^{1}MLCT, the lowest ^{3}MLCT and the doublet are shown.

Table S1 Geometrical parameters of the relaxed Cu(dmp)$_2$ intermediates.

Parameter	S$_0$	^{1}MLCT	^{3}MLCT	D$_0$
bond lengths in Å				
Cu-N(1)	2.044	2.237	1.985	2.006
Cu-N(10)	2.044	2.018	1.985	2.006
Cu-N(1)'	2.044	1.952	1.984	2.006

|				
Cu-N(10)'	2.044	2.025	1.984	2.006
N(1)-C(11)	1.355	1.354	1.371	1.366
N(10)-C(12)	1.355	1.359	1.371	1.366
N(1)'-C(11)'	1.355	1.382	1.371	1.366
N(10)'-C(12)'	1.355	1.386	1.371	1.366
C(11)-C(12)	1.435	1.446	1.411	1.433
C(11)'-C(12)'	1.435	1.408	1.411	1.433
bond angles				
N(1)-Cu-N(10)	82.4	79.7	84.3	84.4
N(1)-Cu-N(1)'	124.5	106.3	108.8	109.8
N(1)-Cu-N(10)'	124.5	124.3	140.9	139.3
N(10)-Cu-N(1)'	124.5	155.1	140.9	139.3
N(10)-Cu-N(10)'	124.5	110.8	108.8	109.8
N(1)'-Cu-N(10)'	82.4	86.1	84.4	84.4
dihedral angles				
ϑ_x	90.0	105.1	90.0	90.0
ϑ_y	90.0	77.1	90.0	90.0
ϑ_z	90.0	65.2	59.7	62.3
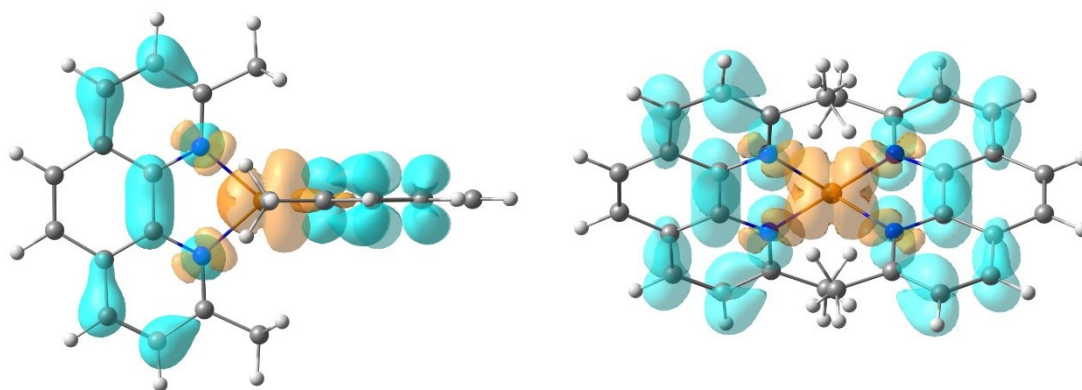
Figure S7 S_3-S_0 difference density (cyan: positive, orange: negative) at the S_0-[Cu(dmp)$_2$]$^+$ geometry. Left: side view, right: top view. The contour value is 0.001.

The first intermediate along the reaction path (**Scheme S2**) is a partially relaxed geometry in the ^{1}MLCT state (**Figure S6**). Recent transient absorption measurements pointed to a 47-75 fs lifetime of this structure.[9,12] It is assumed that this intermediate retains its perpendicular ligand arrangement.[12] Hence, it is a short-lived excited state structure, which undergoes a non-radiative decay to a lower singlet excited state mediated by a conical intersection. Such a rapid conversion can be interpreted as a passage through a peaked conical intersection.[13,14] The excited state minimum that we have obtained from geometry optimization can be assigned to a fully relaxed ^{1}MLCT intermediate. This excited state minimum is

characterized by an oxidized d^9-copper and a phen radical-anion. Such a singlet diradical character is responsible for a difference in geometries of the two phen ligands because the excitation localizes at one of the phen ligands. To understand the localization/delocalization pattern we have analyzed the corresponding orbitals[15] of a triplet diradical wave function (**Figure S8**). One singly occupied MO (SOMO) is based on the d_{xz} orbital of copper, while the other SOMO is of π^*-type delocalized on the phen ligand. From inspection of the latter it becomes apparent that N(1)'-C(11)' and N(10)'-C(12)' should be elongated while C(11)'-C(12)' should be shortened due to anti-bonding and bonding orbital lobes, respectively. Indeed, these changes are confirmed by the geometrical parameters in **Table S1**. Furthermore, we find shortened Cu-N bonds with 1.952 and 2.025 Å at the reduced phen ligand due to the formal 2+ charge of Cu. The oxidation from d^{10} to d^9-copper results also in a flattening of the phen ligands. The dihedral angle ϑ_z between the two phen planes decreases from 90.0° to 62.3°. However, this distortion is accompanied by significant rocking (ϑ_x of 105.1°) and wagging (ϑ_y of 77.1°) of the phen. All these changes are indicative of a preferred five-coordinated copper in the d^9 configuration. The next step of the reaction scheme leads to a ^{3}MLCT state through an intersystem crossing. The structurally relaxed ^{3}MLCT intermediate is modeled by a ^{3}MLCT minimum geometry (**Figure S6**). The geometry of this model is characterized by four equal Cu-N bonds and also both phen structures are identical, which is in line with the spin density in **Figure S9**.
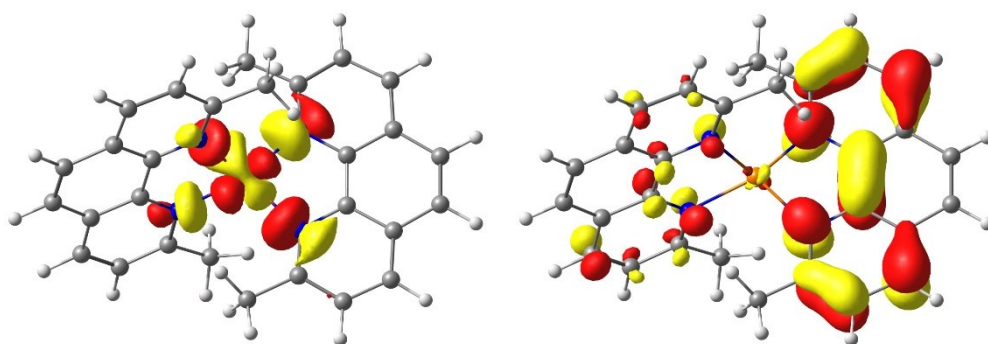

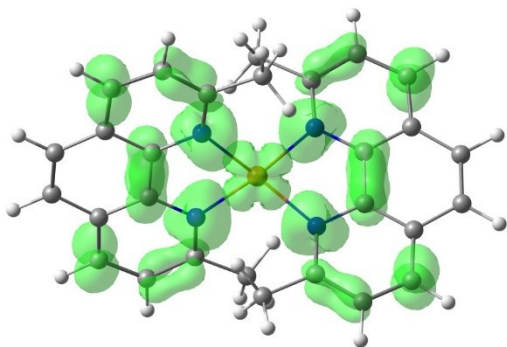**Figure S8** Two SOMOs at the S_1-[Cu(dmp)$_2$]$^+$ geometry. The contour value is 0.04.

Figure S9 Spin density at the ^{3}MLCT-$[Cu(dmp)_2]^+$ geometry. The contour value is 0.002.

In the last step of the reaction scheme (**Scheme S2**) an electron transfer from the ligand to the electron acceptor takes place, which results in a weakly coupled diradical. In our study we model this intermediate with $[Cu(dmp)_2]^{2+}$ in a doublet configuration. The Cu-N bonds of this model are shorter than those of the singlet but slightly longer than those in the triplet. However, the geometry of phen ligand is nearly unchanged from the ground state minimum. Finally, the spin density (**Figure S10**) clearly demonstrates an unpaired electron in the d-orbital of copper. The Mulliken spin population at copper is 65%. The d^9 configuration is responsible for a ϑ_z-value of 62.3° which is close to the singlet and triplet values. The twisting between the phen planes is slightly increased as compared to the triplet geometry by 2.5°. However, there is no rocking or wagging observed, as both ϑ_x- and ϑ_y-angles are 90° (**Table S1**).
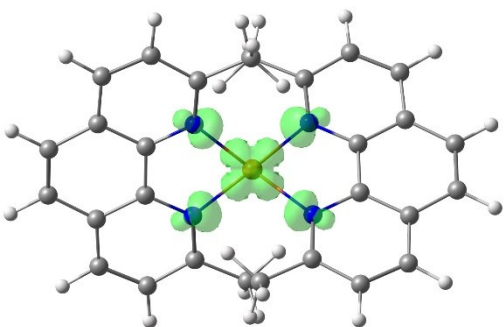

Figure S10 Spin density at the D_0-$[Cu(dmp)_2]^{2+}$ geometry. The contour value is 0.005.

$[Cu(dpp)_2]^+$

The optimized ground state structure of the $[Cu(dpp)_2]^+$ has D_2 symmetry (**Figure S11**). It is characterized by a 62° angle between the phen ligands. This flattening of the tetrahedral coordination is due to the steric bulkiness of the phenyl substituents attached to the phen. We find an interligand π-stacking interaction

between the phenyl and the phen with an off-center arrangement. Due to the π-π interaction the phenyl rings are twisted by 39 degrees from the plane of the phen. Hence, this π-π interaction is more favorable then the intraligand conjugation between the π-system of the phenyl and the phen. Besides the forced flattening this particular geometry is also effectively shielding the Cu(I)-center from a possible coordination by a MeOH solvent molecule as can be seen from the sphere representation of the D_0-structure in **Figure S12**. Thus, the geometry explains the lack of solvent dependence of Cu(dpp)$_2$ in contrast to Cu(dmp)$_2$.
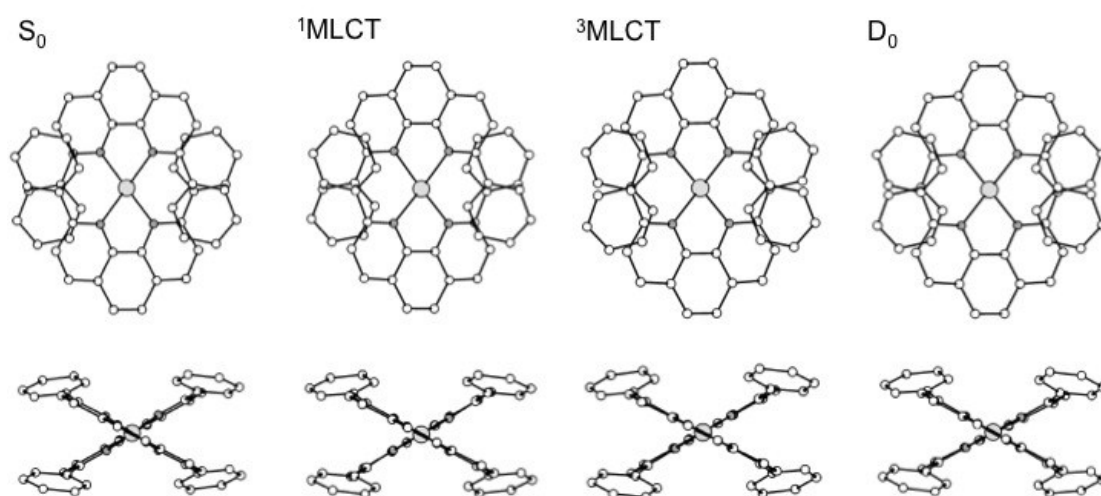

Figure S11 Geometries of the [Cu(dpp)$_2$] model. From the left to the right the minimum of the ground, the lowest ^{1}MLCT, the lowest ^{3}MLCT and the doublet state are shown.
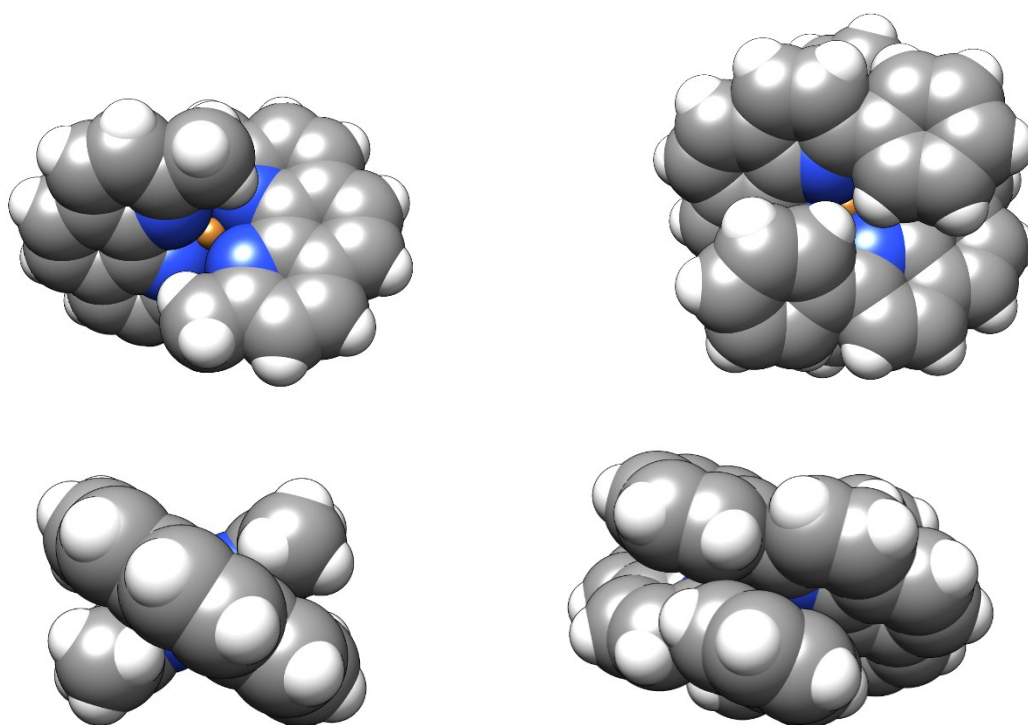
Figure S12 Geometries of the doublet state with d^9 Cu in a sphere representation. Left: [Cu(dmp)$_2$]$^{2+}$ model of ^{Me}C$^+$A$_4$$^{8+}$. Right: [Cu(dpp)$_2$]$^{2+}$ model of ^{Ph}C$^+$A$_4$$^{8+}$.

The brightest excitation in the visible range of [Cu(dpp)$_2$]$^+$ is S$_0 \rightarrow$ S$_5$ with an oscillator strength of 0.04. It is dominated by a one-electron transition from the copper d$_{xz}$ based molecular orbital to a linear combination of π*-orbitals of the phen ligand, as displayed in **Figure S13** along with the difference density. Due to the distortion of the phenyl out of the phen plane the density is mainly delocalized at the phen. In addition also S$_1$, S$_3$ and S$_6$ states have non-negligible oscillator strengths, while for [Cu(dmp)$_2$]$^+$ S$_3$ is the only bright state. This difference in absorption reflects the structural differences in the ground state. The ground state geometry of [Cu(dpp)$_2$]$^+$ has D$_2$ symmetry and is flattened already in contrast to higher symmetry of the [Cu(dmp)$_2$]$^+$.
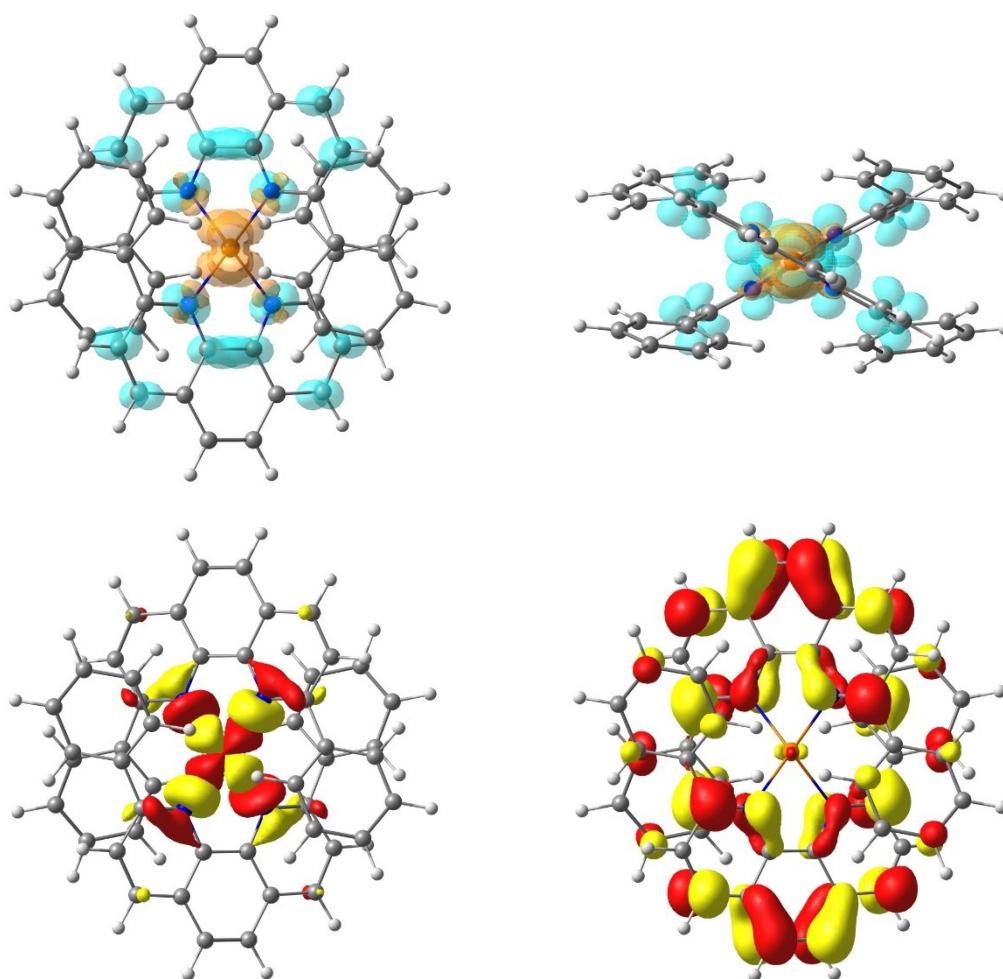
Figure S13 Top: S_5-S_0 difference density (cyan: positive, orange: negative) at the S_0-[Cu(dpp)$_2$]$^+$ geometry from two different perspectives. The contour value is 0.002. Bottom: HOMO (left) and LUMO (right) of [Cu(dpp)$_2$]$^+$. The contour value is 0.03.

An ultrafast decay is also observed for [Cu(dpp)$_2$]$^+$. This decay takes place within 125 fs[16] which is slower than in case of [Cu(dmp)$_2$]$^+$ but is still ultrafast, therefore precluding the formation of a minimum on the S_5 excited state. Hence, our optimization of the singlet excited state represents the relaxed ^{1}MLCT intermediate. The structural parameters collected in **Table S2** show that the two phen ligands are different. While at one phen-ligand the Cu-N bonds are shortened by 0.04 Å, they are lengthened at the other phen-ligand by 0.07 Å. In addition, one ligand has a less pronounced conjugation displayed in the N-C and the C(11)-C(12) bonds, while the other one is nearly unchanged as compared to the S_0-geometry. Further, the dihedral angle of the phenyl group from the phen residue is also different between the two phen-ligands: 45° at phen and remaining 39° at phen'. These geometrical parameters point to the fact that one phen is a radical anion carrying the electron from the copper. This becomes apparent from the

inspection of the molecular orbitals: **Figure S14** shows that the LUMO is a π^*-orbital localized on only one ligand. The shape of this LUMO explains also the reduced conjugation and in particular the shorter C(11)-C(12) bond.
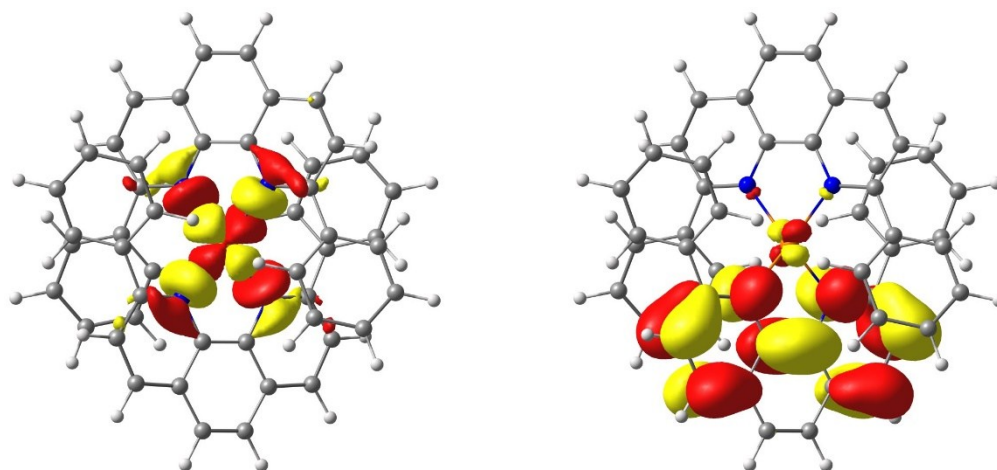

Figure S14 HOMO (left) and LUMO (right) at the S_1-[Cu(dpp)$_2$]$^+$ geometry. The contour value is 0.03.

   The oxidation of copper from d^{10} to d^9 gives rise to a flattening of the complex which is of minor extent compared to the Cu(dmp)$_2$. The ϑ_z-angle decreases by 7° when going from S_0 to S_1 (**Table S2**). The next relaxed intermediate, which is formed after the ISC is the optimized triplet model (**Figure S11**). It has marginally shorter Cu-N and C(11)-C(12) bonds on one phen-ligand than on the other. There is also a negligible difference of 1° in the phenyl-phen torsion between the two ligands. The spin density is found on Cu and widely distributed on phen but not at the phenyl (**Figure S15**). Finally, the model of the CT state resembles the trends observed for the [Cu(dmp)$_2$]-complex. The Cu-N bonds are in-between those of the singlet and triplet model. However, the phen geometry deviates slightly from the singlet case. The spin density in **Figure S16** affirms that the unpaired electron is residing on copper with a small contribution from the adjacent N atoms.

Table S2 Geometrical parameters of the relaxed Cu(dpp)$_2$ intermediates.

Parameter	S_0	^{1}MLCT	^{3}MLCT	D_0
bond lengths in Å				
Cu-N(1)	2.055	2.012	1.986	2.007
Cu-N(10)	2.055	2.012	1.986	2.008
Cu-N(1)'	2.056	2.127	1.989	2.008

|				
Cu-N(10)'	2.054	2.126	1.988	2.007
N(1)-C(11)	1.356	1.379	1.370	1.360
N(10)-C(12)	1.356	1.379	1.370	1.360
N(1)'-C(11)'	1.356	1.355	1.370	1.360
N(10)'-C(12)'	1.356	1.355	1.370	1.360
C(11)-C(12)	1.446	1.411	1.421	1.434
C(11)'-C(12)'	1.446	1.444	1.422	1.434
bond angles				
N(1)-Cu-N(10)	82.9	84.7	84.9	84.2
N(1)-Cu-N(1)'	113.3	110.4	108.0	108.9
N(1)-Cu-N(10)'	137.0	141.6	141.5	141.1
N(10)-Cu-N(1)'	136.8	141.6	141.3	141.0
N(10)-Cu-N(10)'	113.0	110.4	107.9	108.8
N(1)'-Cu-N(10)'	82.9	79.9	84.9	84.2
dihedral angles				
ϑ_x	90.0	90.0	90.0	89.9
ϑ_y	90.2	90.0	90.1	90.1
ϑ_z	67.4	59.8	58.7	59.7
phi	140.9	135.0	138.3	140.2
	140.6	135.2	137.9	140.2
	140.9	141.1	138.7	140.2
	140.6	141.0	138.8	140.2
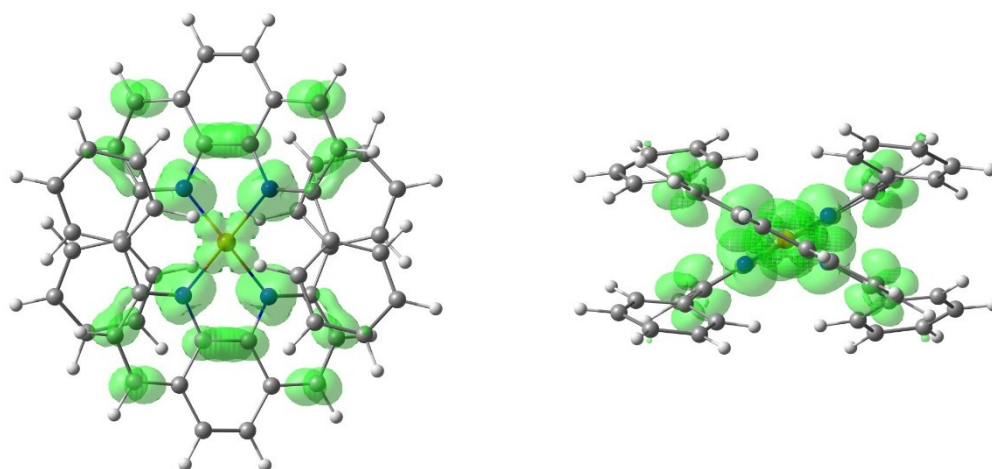
Figure S15 Spin density at the ^{3}MLCT-[Cu(dpp)$_2$]$^+$ geometry. The contour value is 0.002.
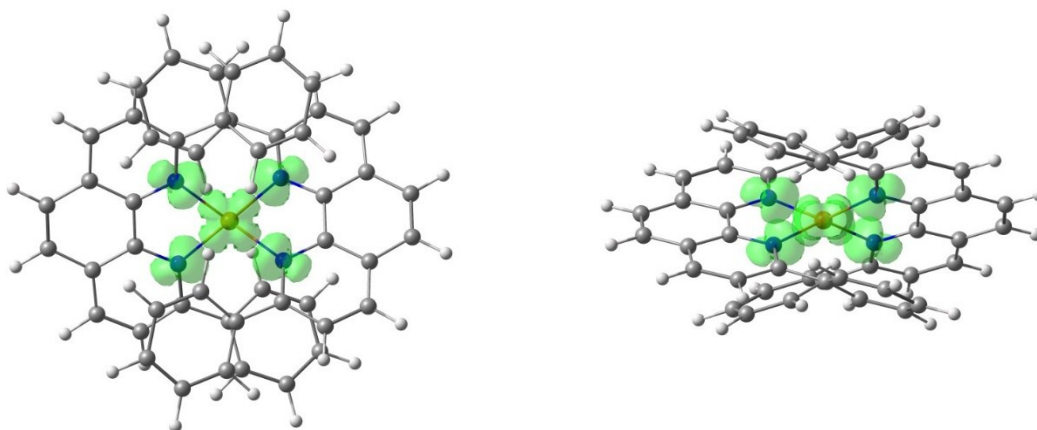
Figure S16 Spin density at the D_0-[Cu(dpp)$_2$]$^{2+}$ geometry. The contour value is 0.002.

Calculation of EPR parameters

In addition to the *ab initio* multireference calculations we have computed the *g* values and the hyperfine coupling constants using DFT. For the DFT calculation of magnetic properties the same B3LYP functional was used owing to its reasonable performance as documented in ref.17,18. To account for the relativistic effect we have used the second-order Douglas-Kroll-Hess (DKH-2) transformation including the picture-change effect.[19] Especially for hyperfine coupling constants the use of DKH-2 operators instead of their non-relativistic counterparts has been found to be crucial to obtain meaningful results.[20] Further, we have used a Gaussian finite-size nucleus model instead of a point charge model to take into account the different extent of charge and magnetization distribution.[20,21] The CP(PPP) basis set was adapted for copper which is a more accurate triple-ξ basis with more flexibility in the core region. Hence, it is expected that this choice will improve the Fermi contact contribution of the hyperfine coupling tensor. In addition, larger integration grid in the radial part was chosen for copper to ensure accurate numerical integration in the core region in the presence of very steep basis functions.[22]

The performance of B3LYP for the calculations of *g* values was evaluated for a number of copper complexes. A systematic underestimation of the out of plane component by up to a factor of 2 was observed and its origin has been rationalized.[17] This underestimation leads to large errors in the dominating value of the copper hyperfine coupling tensor, owing to the significantly lowered spin-orbit component. To overcome this deficiency the correction shown in eq 1 involving the experimental $\Delta g_{||}$ value was suggested by Sinnecker et al.:[23]

$$A_{\parallel}^{(so)}(\text{corrected}) = A_{\parallel}^{(so)}(\text{DFT}) \frac{\Delta g_{\parallel}^{\text{experimental}}}{\Delta g_{\parallel}^{DFT}}$$ **(S1)**

Such a correction was successfully applied to plastocyanin[23] as well as type zero copper proteins.[24] Hence, we will also make use of this correction in the present study.

_g_-tensor

The theoretical g-values along with the directions of the principal axes of the g-tensor for $[Cu(dmp)_2]^{2+}$ and $[Cu(dpp)_2]^{2+}$, are given in **Table S3** and **Figures S17** and **S18**, respectively. For both complexes, the g_3 principal axis is the unique molecular axis which bisects the largest of the N-Cu-N bond angles of 139.3° in case of $[Cu(dmp)_2]^{2+}$ and 141.0° in case of $[Cu(dpp)_2]^{2+}$. For all methods, the g-matrix of $[Cu(dpp)_2]^{2+}$ is found to be closer to axial symmetry than for $[Cu(dmp)_2]^{2+}$. The deviation between the g_1 and g_2 values at the DFT level is 0.0004 for $[Cu(dpp)_2]^{2+}$ and 0.0087 for $[Cu(dmp)_2]^{2+}$. However, the deviation is larger at the NEVPT2 level. At the SORCI level of theory, which is only available for the smaller $[Cu(dmp)_2]^{2+}$ complex, the deviation from axial symmetry is intermediate between that of DFT and NEVPT2.

While the experimental $g_\perp$ value for $[Cu(dpp)_2]^{2+}$ is in quantitative agreement with the calculated g_1 and g_2 values at the DFT level, the experimental $g_{||}$ (g_3) value is underestimated by as much as 0.18. The origin of this 2-fold underestimation of the difference between $g_{||}$ and $g_\perp$ is widely recognized to be systematic in DFT calculations.[17] The QDPT approach with NEVPT2 energies yields a $g_{||}$ value of 2.4547, which is in better agreement with experiment, albeit somewhat too large. However, not only the $g_{||}$ value, but all g-tensor components are overestimated. Compared to the experimental values, the g_3 value is larger by 0.085, while g_1, and g_2 are overestimated by 0.005 and 0.0073, respectively. The systematically higher g-tensor values might originate from the inconsistency of the CASSCF/NEVPT2 approach because the spin orbit coupling (SOC) contribution is calculated using the SA-CASSCF wave function, while the denominator in the QDPT expression utilizes NEVPT2 corrected energies. The SORCI method is more consistent due to the equal treatment of SOC contribution and excitation energies, and it also recovers a larger part of the differential dynamic correlation between the ground and the excited states in comparison to NEVPT2. Thus, despite SORCI calculations being based on the same zeroth-order wave function as the NEVPT2, we can expect the g values to be in better agreement with the experiment. The conceptual superiority of

SORCI for g-tensor calculations was previously demonstrated for Cu(II) model complexes.[25,26] However, due to the large size of the $[Cu(dpp)_2]^{2+}$ complex a SORCI calculation was not feasible. Nevertheless, we have studied the smaller complex $[Cu(dmp)_2]^{2+}$. As can be seen in **Table S3**, the differences of the g-tensor components between the two complexes are below 0.008 at the DFT and at the CASSCF/NEVPT2 level of theory. This small difference in the g tensor can be attributed to the approximate congruence of the CuN4 core in both complexes (see geometrical parameters in **Tables S1** and **S2**). Hence, we can also expect that the g-values of $[Cu(dmp)_2]^{2+}$ are very close to those of $[Cu(dpp)_2]^{2+}$ which justifies the comparison of the SORCI results of the former with the experimental values of the latter. This comparison shows that SORCI considerably improves the results: the calculated g_3 value is only 0.012 higher than the experimental one while g_1 and g_2 are 0.020 and 0.043 above the experimental values. It is gratifying to see this improvement, considering that the difference of g values between the two complexes is of similar size as the deviation between SORCI and the experimental values.

Table S3. Calculated g values for $[Cu(dmp)_2]^{2+}$ and $[Cu(dpp)_2]^{2+}$ models.

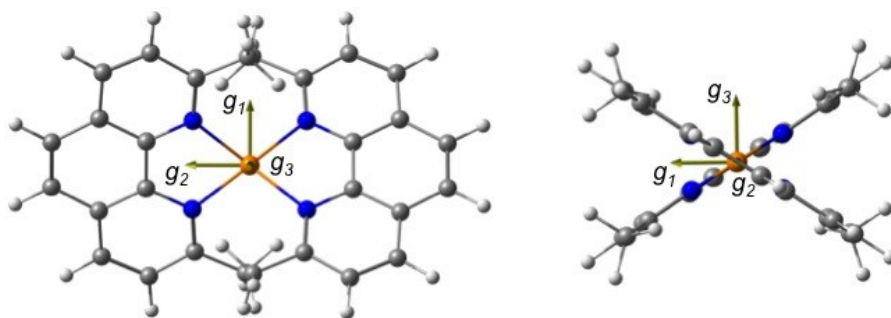| Model	DFT	NEVPT2	SORCI	experiment [27]
$[Cu(dmp)_2]^{2+}$				
g_1 $(g_{\perp,1})$	2.0605	2.1173	2.0901	
g_2 $(g_{\perp,2})$	2.0692	2.1502	2.1132	
g_3 $(g_{\parallel})$	2.1891	2.4599	2.3827	
g_{iso}	2.1062	2.2424	2.1953	
$[Cu(dpp)_2]^{2+}$				
g_1 $(g_{\perp,1})$	2.0668	2.1202		2.07
g_2 $(g_{\perp,2})$	2.0672	2.1434		
g_3 $(g_{\parallel})$	2.1943	2.4547		2.37
g_{iso}	2.1095	2.2394		

Figure S17. Principal axes of the calculated g-tensor for the D_0-[Cu(dmp)$_2$]$^{2+}$ structure.
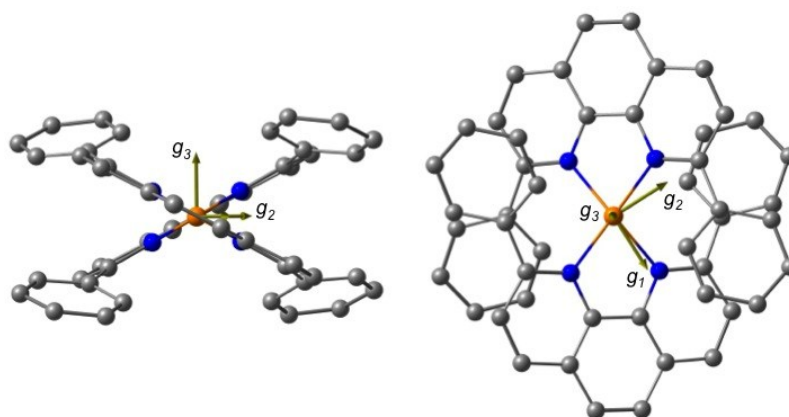

Figure S18 Principal axes of the calculated g-tensor for the D_0-[Cu(dpp)$_2$]$^{2+}$ structure. The hydrogens are left out for clarity.

Hyperfine coupling constants

The hyperfine coupling constants (HFC) for the copper in [Cu(dmp)$_2$]$^{2+}$ and [Cu(dpp)$_2$]$^{2+}$ are collected in **Table S4**. We find the values similar for both complexes with a difference of only 2 MHz between the isotropic A-value. This is in accordance with the similarity already observed for the g-tensor, due to the nearly identical local coordination of the copper. The principal value A_1 along the unique molecular axis (**Figures S19** and **S20**) is negative while the other two values are positive. Overall the HFC-tensor is nearly axial which is again in line with the g-tensor analyzed above. Hence, in the following, the composition of HFC can be discussed in general for both complexes.

The three contributions to the HFCs are the Fermi-contact term (fc), the spin dipolar contribution (sd), and the spin-orbit term (so). In order to understand the change of sign for the principal values further analysis is provided in **Table S4**. The total negative value of the HFCs can be traced back to the largely negative A_1 value. The decomposition of A_1 reveals a negative $A^{(fc)}$ and $A^{(sd)}$ contribution while the $A^{(so)}$ component is positive. The negative $A^{(fc)}$ term can be rationalized as a result of spin polarization induced

by the unpaired electron at the copper. This spin polarization leads to a larger spin density of β- than α-electrons. Such a "negative spin-density" is responsible for the negative sign. The A_1 value is -16.7 mT for [Cu(dpp)$_2$]$^{2+}$ which is in good agreement with the experimental value of A$_{||}$ 17.7 MHz.[27] Such a coincidence with the experiment is due to fortunate error compensation from different contributions. The underestimation g shift by the DFT is related to the spin-orbit contribution $A^{(so)}$. Hence, it is reflected in a too small $A^{(so)}$ value. A simple scaling of this spin-orbit contribution is done to address this shortcoming:[23,24]

$$A_{||}^{(so)}(\text{corrected}) = A_{||}^{(so)}(\text{DFT}) \frac{\Delta g_{||}^{\text{experimental}}}{\Delta g_{||}^{DFT}} \qquad \textbf{(S1)}$$

Using the SORCI $g_{||}$ shift for [Cu(dmp)$_2$]$^{2+}$ and the experimental value for [Cu(dpp)$_2$]$^{2+}$ results in a scaling by a factor of 2. The corrected A$_{||}$ values are -7.3 and -8.7 MHz for [Cu(dmp)$_2$]$^{2+}$ and [Cu(dpp)$_2$]$^{2+}$, respectively. After the correction the agreement with experiment significantly worsens for the $A_{||}$ value of [Cu(dpp)$_2$]$^{2+}$. The largest deviation must come from the $A_{||}^{(fc)}$ contribution.

In case of A_2 and A_3 a correction of the spin-orbit contribution is not necessary as the corresponding g values are in good agreement with the experimental counterparts. In contrast to A_1 the $A^{(sd)}$ contribution becomes positive and of similar magnitude as $A^{(fc)}$. Hence, both A_2 and A_3 are positive. However, due to its small size an experimental value could not be determined.

Table S4 Calculated Cu(II) A-tensor for [Cu(dmp)$_2$]$^{2+}$ and [Cu(dpp)$_2$]$^{2+}$ models in mT.

[Cu(dmp)$_2$]$^{2+}$	A_1 ($A_{||}$)	A_2 ($A_{\perp,1}$)	A_3 ($A_{\perp,2}$)	A_{iso}
$A^{(fc)}$	-8.78	-8.78	-8.78	
$A^{(sd)}$	-16.24	8.17	8.07	
$A^{(so)}$	8.74 (17.77)*	3.60	03.03	
A(total)	**-16.27 (-7.28)***	**03.00**	**02.32**	**-3.7 (-0.65)***
[Cu(dpp)$_2$]$^{2+}$				
$A^{(fc)}$	-8.82	-8.82	-8.82	
$A^{(sd)}$	-16.67	8.39	8.28	
$A^{(so)}$	8.78 (16.77)*	3.43	03.14	
A(total)	**-16.70 (-8.71)***	**03.00**	**02.61**	**-3.7 (-1.0)***
experiment[27]	17.7			

*corrected spin-orbit contribution after scaling is given in brackets.
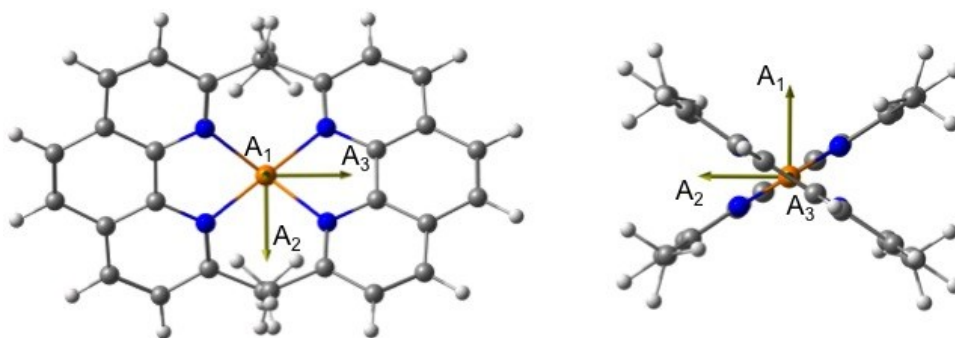

Figure S19 Principal axes of the calculated A-tensor for the D_0-$[Cu(dmp)_2]^{2+}$ structure.
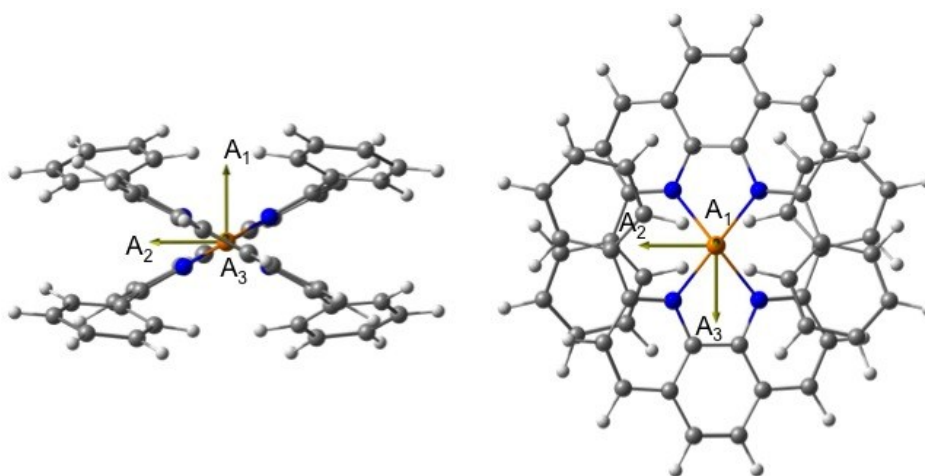

Figure S20 Principal axes of the calculated A-tensor for the D_0-$[Cu(dpp)_2]^{2+}$ structure.

The HFC tensors of nitrogen in $[Cu(dmp)_2]^{2+}$ and $[Cu(dpp)_2]^{2+}$ are given in **Table S5**. The coupling constants are much smaller than those of copper, which is due to the lighter core, smaller polarization at the core level and a negligible $A^{(so)}$ contribution (it is omitted from **Table S5** because it is below 1 MHz=0.036 mT).[18,28] Both complexes have four coordinating nitrogens which are expected to have pairwise identical HFC tensors due to the D_2 symmetry. However, we find a deviation below 0.05 MHz (0.0018 mT) between the different nitrogen for each complex. Hence, we limit the discussion to one of the nitrogens for each complex. Moreover, the differences between nitrogen's HFC in $[Cu(dmp)_2]^{2+}$ and $[Cu(dpp)_2]^{2+}$ are below 1 MHz (=0.036 mT). Hence, in the following we discuss results independent of the complex. The $A^{(fc)}$ is the largest contribution to nitrogen's HFC: 0.89-0.93 mT. Its value is positive in contrast to the largely negative value in copper. This difference is not surprising because the nature of the interaction is quite different: the isotropic contribution of nitrogen is dominated by the direct valence

contribution, while in copper it is based on core-level spin-polarization.[26] The $A^{(sd)}$ contribution is 0.21 to 0.25 mT for $A_{||}$ and -0.11 to -0.14 mT for $A_\perp$. Since the spin-orbit contribution is below 1 MHz it can be neglected and the total $A_{||}$ and $A_\perp$ values are 1.14 to 1.18 mT and 0.75 to 0.79 mT. Due to lack of experimental data in the literature a comparison to measured HFC is not possible.

Table S5 Calculated ^{14}N A-tensor for $[Cu(dmp)_2]^{2+}$ and $[Cu(dpp)_2]^{2+}$ models in mT.

$[Cu(dmp)_2]^{2+}$	A_1 ($A_{||}$)	A_2 ($A_{\perp,1}$)	A_3 ($A_{\perp,2}$)	A_{iso}
$A^{(fc)}$	0.93	0.93	0.93	
$A^{(sd)}$	0.25	-0.11		
A(total)	**1.18**	**0.82**	**0.79**	**0.89**
$[Cu(dpp)_2]^{2+}$				
$A^{(fc)}$	0.89	0.89	0.89	
$A^{(sd)}$	0.21	-0.11	-0.14	
A(total)	**1.14**	**0.79**	**0.75**	**0.89**

E. Theoretical calculation of CT decay time

Solving the set of differential equations (1) in the main text, in general yields a tri-exponential function.

$$f(t) = A_1 \exp(-t/\tau_1) + A_2 \exp(-t/\tau_2) + A_3 \exp(-t/\tau_3) \tag{S2}$$

However, for the relevant range of kinetic parameters, the slowest of the exponential components represents an amplitude fraction of more than 80 percent. To compare the theoretical with the experimental results, an effective mono-exponential decay time τ_{eff} was determined by choosing τ_{eff} such that the integrated square deviation between the tri-exponential and the effective mono-exponential curve was minimized. Thus, the following equation was obtained for τ_{eff}

$$A_1 \frac{\tau_1^2}{\left(\tau_1 + \tau_{\mathrm{eff}}\right)^2} + A_2 \frac{\tau_2^2}{\left(\tau_2 + \tau_{\mathrm{eff}}\right)^2} + A_3 \frac{\tau_3^2}{\left(\tau_3 + \tau_{\mathrm{eff}}\right)^2} - \frac{1}{4} = 0 \tag{S3}$$

which was solved numerically. The result thereby obtained was very close to one obtained by a simpler relation, based upon the assumption that the time integrals over the tri-exponential and the effective mono-exponential decay curves should be equal:

$$\int_0^\infty \sum A_i \exp(-t / \tau_i)dt = \int_0^\infty \exp(-t / \tau_{\mathrm{av}})dt \tag{S4}$$

This condition results in the equation

$$\tau_{av} = \sum A_i \tau_i \tag{S5}$$

In **Figure S21** the resulting mono-exponential decay curves are shown for a set of characteristic field values.
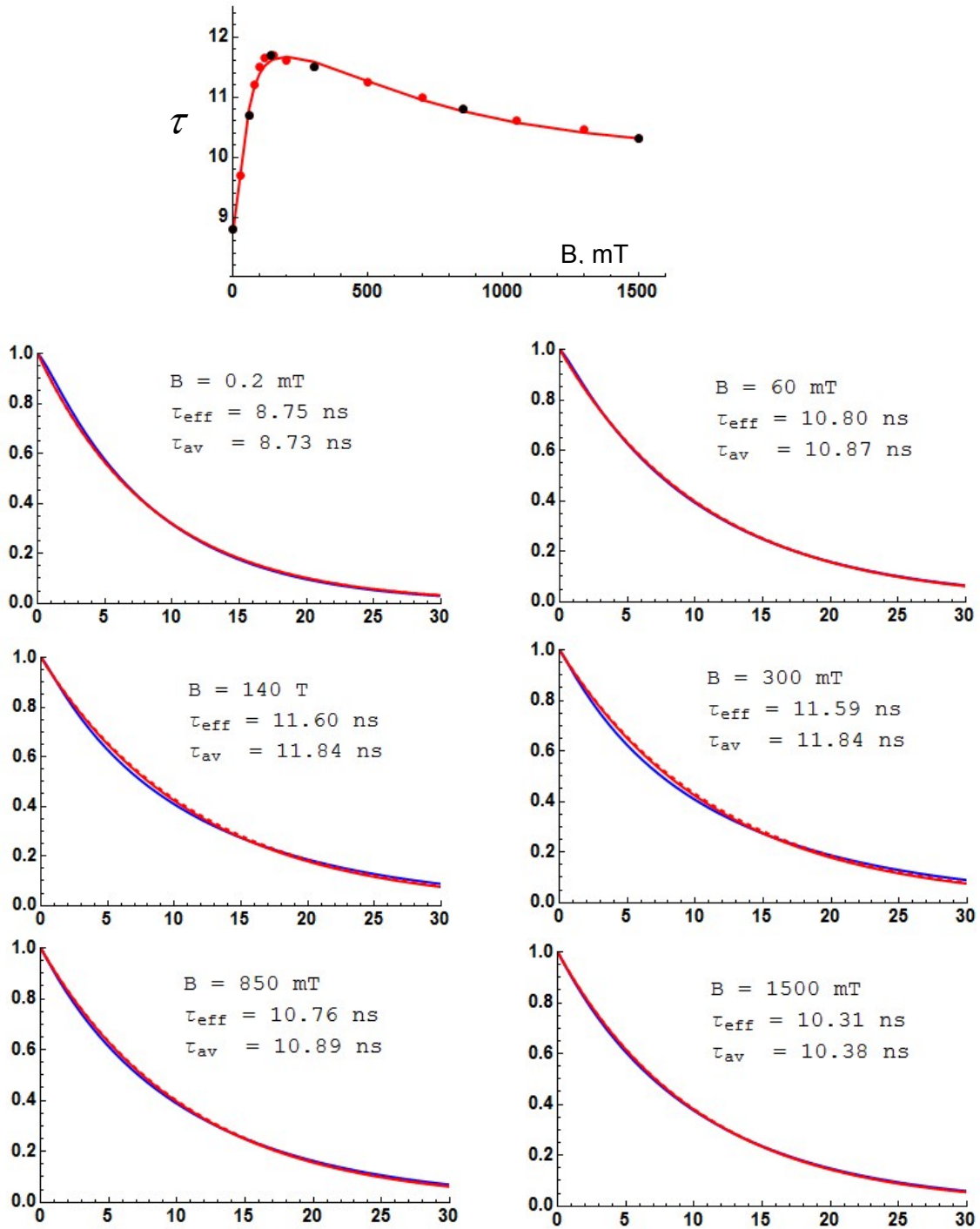
Figure S21 Quality of fit when replacing the tri-exponential decay by a mono-exponential one. The fields selected correspond to the data points marked in black in the fit of the experimental data shown in the first diagram in the center. Horizontal axis of the 6 decay traces: time, ns. Blue: tri-exponential decay, solid red: mono-exponential decay with decay time calculated by eq (S3) dashed red: mono-exponential decay with decay time calculated by eq (S5).

F. Refined Analysis of McMillin Scheme

In a paper published in 1983 by McMillin and coworkers,[29] the temperature dependence of emission yield and life time of various copper(I) phenanthroline and bipyridine complexes were analyzed in terms of an equilibrium between ^{1}MLCT and ^{3}MLCT state based on **Scheme 3**. Here we are extending this analysis for the $[Cu(dmp)_2]^+$ complex making further use of experimental data published more recently,[30] which is discussed below.
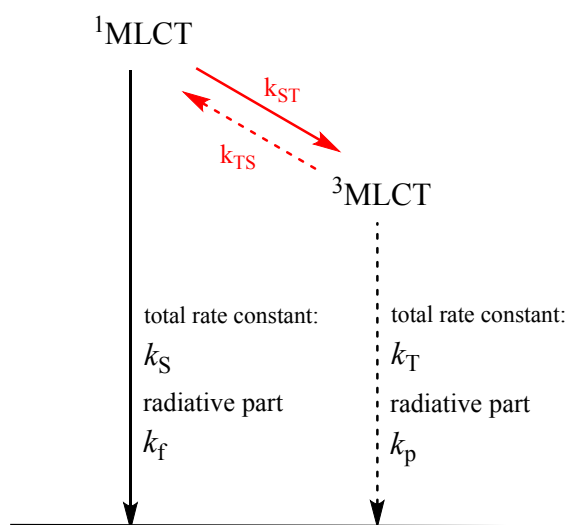
Scheme S3 Kinetic scheme describing MLCT state conversion and decay in $Cu(I)(phen)_2^+$ complexes according to McMillin and coworkers.[29]

In the analysis in Ref.[29] , it was assumed that the equilibrium between ^{1}MLCT and ^{3}MLCT is fully established while observing the emission. However, since both the temperature dependent data of ϕ_e and τ_e are given separately, the quantitative data analysis can be carried further without making the assumption of a fully established ISC equilibrium. Recent fs-time-resolved experiments by Iwamura et al.[31] have revealed that for ^{1}MLCT photoexcited $[Cu(dmp)_2]^+$ the Jahn-Teller relaxation from D_{2d} geometry, where the two phenanthroline ligands are nearly perpendicular, to a flattened D_2 geometry occurs within about 0.8 ps, which is followed by a fast ISC process to ^{3}MLCT within about 10 ps. The latter value is in agreement with a previous observation by Siddique et al.[30] and with more recent work by Castellano and coworkers.[32] That the quantum yield of prompt emission from ^{1}MLCT corresponds to approximately 1/7 of the quantum yield of stationary emission represents an additional useful piece of information.[30]

Based on the kinetic equations resulting from **Scheme 3,** the following relation can be derived.

$$\phi_e = \phi_f + \phi_p$$
$$= k_f \frac{k_{TS} + k_T}{k_{TS}k_S + k_{ST}k_T + k_Sk_T} + k_p \frac{k_{ST}}{k_{TS}k_S + k_{ST}k_T + k_Sk_T} \tag{S6}$$

where ϕ_f denotes the yield of all quanta emitted from ^{1}MLCT, ϕ_p the yield of all quanta emitted from ^{3}MLCT, k_S and k_T the overall decay constants of ^{1}MLCT and ^{3}MLCT, and k_{ST} and k_{TS} the ISC rate constants from ^{1}MLCT to ^{3}MLCT and vice versa, respectively.

The time dependent solution of formation and decay of ^{1}MLCT and ^{3}MLCT state is represented as a bi-exponential function, with decay times in the 10 ps and the 100 ns range. Only the slower component was measured in Ref.29. The analytical solution for the longer lifetime is given by

$$\tau_e = 2\left(k_S + k_T + k_{ST}(1+K) - \sqrt{(k_{ST} + k_S)^2 + 4k_{ST}^2 K - 2(k_{ST} + k_S)(k_T + k_{ST}K) + (k_T + k_{ST}K)^2}\right)^{-1} \tag{S7}$$

It can be adopted from the well know solution of excimer kinetics which is of the same type as **Scheme 3**.

As described by Kirchhoff et al.,[29] the equilibrium constant K defined as

$$K \equiv \frac{k_{TS}}{k_{ST}} \tag{S8}$$

is calculated by

$$K = \frac{1}{3}\exp\left[\frac{-\Delta E}{kT}\right] \tag{S9}$$

with ΔE describing the singlet/triplet energy gap. In their analysis, Kirchhoff et al.[29] used the approximation that the ratio k_T / k_{ST} is negligible in comparison to K. In that case, fitting the temperature dependence of ϕ_e / τ_e, yields k_f and k_p without any additional assumption. On the other hand, since an experimental value of k_{ST} is known, the temperature dependence of τ_e according to the exact eq(S7) can be used to fit k_T and k_S, if these parameters and k_{ST} are assumed to be temperature independent in the experimental range between 298 and 244 K (cf. **Figure S22**). With the k_T value thus determined, and the

experimental value of k_{ST}, eq (S6) to eq (S7) can be used for the fit of ϕ_e / τ_e (cf. **Figure S23)** without recourse to the approximation applied in Ref.[29]).

The temperature dependent fits were carried out with various values of ΔE ranging between 1600 cm^{-1} and 1300 cm^{-1}. McMillin and coworkers used a value of 1800 cm^{-1} but conceded a 20% uncertainty for that value. Siddique et al.,[30] based on spectral evidence and quantum chemical calculations, also supported such a value of ΔE. As follows from our analysis, such a value is not compatible with the set of temperature dependent data on ϕ_e and τ_e given in Ref.29. Although the quality of the fits of τ_e (*T*) and ϕ_e/τ_e is hardly dependent on the value of ΔE, the formal contribution of phosphorescence would turn to negative values for $\Delta E > 1653$ cm^{-1}. For the ratio of stationary to prompt fluorescence intensity, a marked dependence on ΔE is obtained. The fit parameter values to be selected for the various ΔE are listed in **Table S6**. The experimental ratio of about 1:7 is reproduced for $\Delta E = 1350$ cm^{-1}.
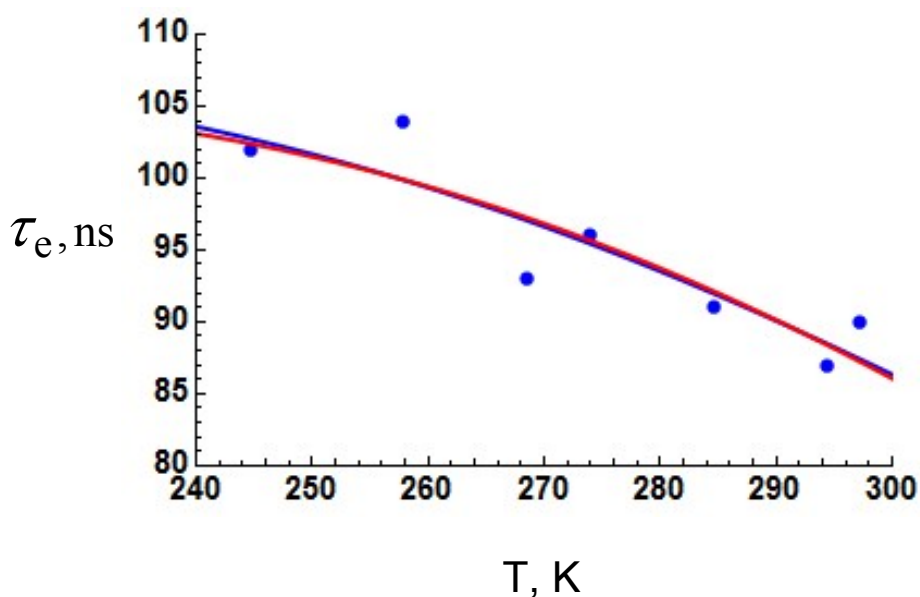

Figure S22 Fit of temperature dependent emission life time data for [Cu(dmp)$_2$]$^+$ from Kirchhoff et al.[29] using equation (S7). Blue curve for $\Delta E = 1350$ cm^{-1} with $k_S = 4.97$ ns^{-1} and $k_T = 0.0092$ ns^{-1}; red curve for $\Delta E = 1600$ cm^{-1} with $k_S = 17.2$ ns^{-1} and $k_T = 0.0094$ ns^{-1}.
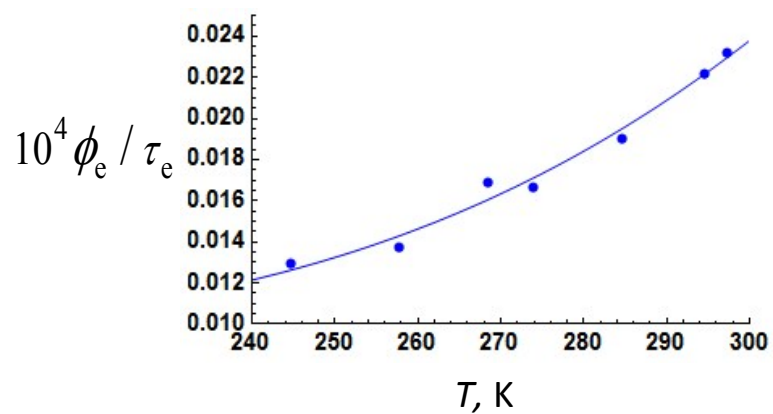
$$10^4 \phi_e / \tau_e$$

Figure S23 Fitting k_f and k_p to simulate the temperature dependence of ϕ_e/τ_e using equations (S6) to (S9) with ΔE = 1350 cm^{-1}. The best fit values are k_f = 3.0×10^6 s^{-1} and k_p = 7.0×10^2 s^{-1}. For values of other parameters cf. **Table S6**.

Table S6 Parameter values and quantum yields[a] based on best fits of $\tau[T]$ and $\phi/\tau[T]$, assuming $k_{ST} = 100$ ns^{-1} and $k_A = 3.2$ ns^{-1}.

ΔE	$1/K[24.1^oC]$	k_S	k_T	k_f	k_p	$\phi_{f,prompt}$	ϕ_f	ϕ_p	ϕ_e	$\phi_e/\phi_{f,prompt}$	ϕ_{CT}	%^{1}CT
cm^{-1}		ns^{-1}	ns^{-1}	ns^{-1}	ns^{-1}	10^{-4}	10^{-4}	10^{-4}	10^{-4}			%
1600	7007	17.2	0.0094	0.0104	$2.51\times10^{-7[b]}$	0.89	1.83	0.19	2.01	2.27	0.85	3.1
1400	2657	6.30	0.0092	0.0038	6.64×10^{-7}	0.36	1.46	0.55	2.01	5.61	0.94	3.1
1360	2191	5.21	0.0092	0.0031	6.93×10^{-7}	0.30	1.43	0.58	2.00	6.72	0.95	3.2
1350	2085	4.97	0.0092	0.0030	6.99×10^{-7}	0.29	1.42	0.58	2.01	7.03	0.95	3.2
1300	1637	3.94	0.0091	0.0024	7.18×10^{-7}	0.23	1.40	0.60	2.00	8.78	0.96	3.2

[a] The various quantum yields refer to prompt emission ($\phi_{f,prompt}$), total emission from ^{1}MLCT (ϕ_f), total emission from ^{3}MLCT (ϕ_p), total emission (ϕ_e). The quantum yield of CT-state formation on reaction with an appended acceptor is denoted ϕ_{CT}, of which a percentage %^{1}CT is formed with singlet spin multiplicity. All quantum yields refer to 24.1^{o}C. [b]The contribution of phosphorescence drops to zero if $\Delta E \approx 1653$ cm^{-1} and becomes formally negative for higher values.
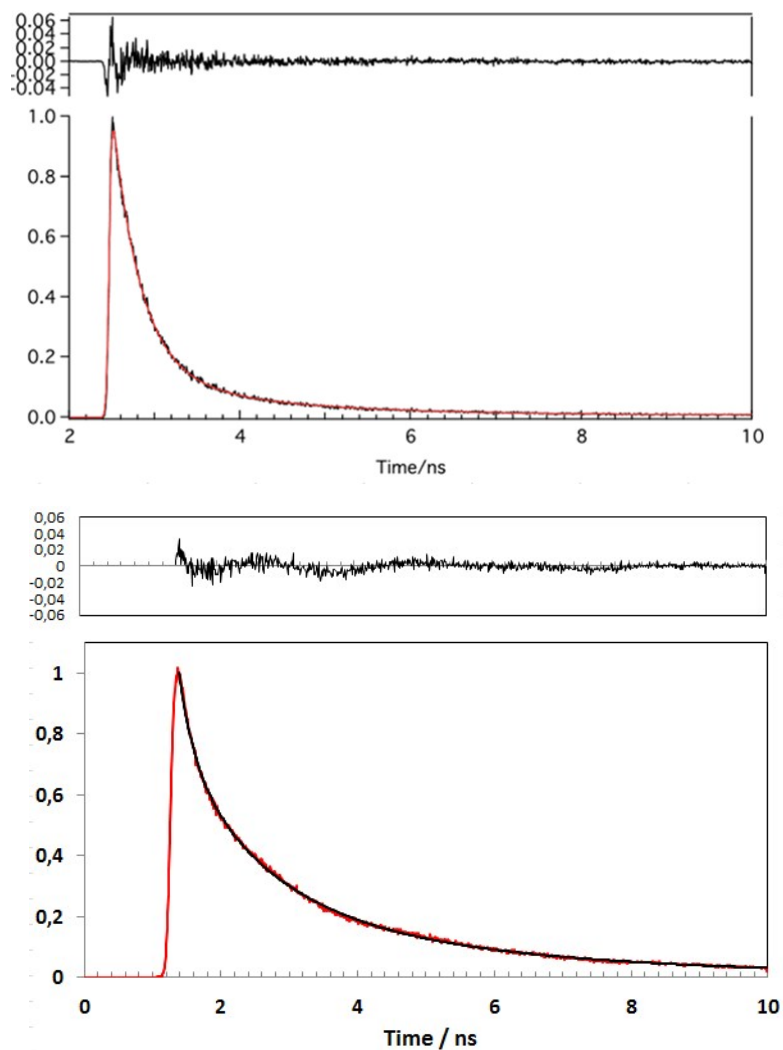
G. Emission decay curves

Figure S24 Emission decay curves for $^{Ph}C^+A_4^{8+}$ (upper panel) and $^{Me}C^+A_4^{8+}$ (lower panel) with tri-exponential fit curves and residuals. The decay times are 0.32 ns (84%), 1.25 ns (15%) and 10.3 ns (1%) in case of $^{Ph}C^+A_4^{8+}$ and 0.22 ns (25%), 1.23 ns (51%) and 4.13 ns (24%) in case of $^{Me}C^+A_4^{8+}$

It is assumed that the multi-exponential decay results from an inhomogeneity of the emissive species concerning the conformations of the side arms and/or association with counter ions (cf. RESULTS in the main text).

H. Spin motion and spin relaxation

Spin relaxation

Within the Redfield approach, the following equations are valid for electron spin relaxation due to rotational modulation of an anisotropic g-tensor and of anisotropic hyperfine coupling to a nuclear spin[33]

$$\frac{1}{T_1} = \frac{1}{20}\left(\Delta A_\omega^2 \left(7I_N\left(1+I_N\right) - m_I^2\right) - 4m_I\Delta A_\omega\Delta g\omega_0 + \frac{2}{3}\Delta g^2\omega_0^2 \right)\frac{\tau_r}{\left(1+\tau_r^2\omega_0^2\right)} \tag{S10}$$

$$\frac{1}{T_2} = \frac{1}{5}\left[\begin{array}{l} \left(\frac{1}{8}\Delta A_\omega^2\left(3I_N\left(1+I_N\right)+5m_I^2\right) - \frac{2}{3}m_I\Delta A_\omega\Delta g\omega_0 + \frac{1}{9}\Delta g^2\omega_0^2\right)\tau_r \\ +\left(\frac{1}{8}\Delta A_\omega^2\left(7I_N\left(1+I_N\right)-m_I^2\right) - \frac{1}{2}m_I\Delta A_\omega\Delta g\omega_0 + \frac{1}{12}\Delta g^2\omega_0^2\right)\frac{\tau_r}{1+\tau_r^2\omega_0^2} \end{array} \right] \tag{S11}$$

Here I_N is the quantum number of total nuclear spin and m_I the magnetic axial quantum number, ΔA_ω is the hyperfine anisotropy in frequency units:

$$\Delta A_\omega = \gamma_e\left(A_P - A_\perp\right) \tag{S12}$$

with γ_e the gyromagnetic ratio of the electron, Δg the g-tensor anisotropy

$$\Delta g = g_P - g_\perp \tag{S13}$$

and ω_0 the Larmor frequency. The rotational correlation time τ_r can be estimated by the Debye-Einstein equation

$$\tau_r = \frac{4\pi\eta}{kT}R^3 \tag{S14}$$

with η the solvent viscosity and R the effective hydrodynamic radius of the complex. For difluorobenzene, the viscosity at room temperature was determined as 0.62×10^{-3} Pa·s.

The effective hydrodynamic radius can be estimated by relating the Connolly surface of the complex into the radius of a sphere.[34] The Connolly surface obtained by Chem3D pro 14.1 from the structure given in **Figure 7** of the main text amounts to 1360 Å^2 yielding an effective radius R of 10.4 Å. From these data a value of 0.71 ns is obtained for τ_r.

To calculate T_1 and T_2, equations (S10) and (S11) have to be averaged over the nuclear quantum numbers of Cu. At zero field, the following values are obtained:

$$T_1(0) = 0.086\,\text{ns} \qquad T_2(0) = 0.1\,\text{ns}$$

Both of these values are significantly smaller than the value of τ_r, meaning that the Redfield condition is violated and the equations are not applicable. The field dependence of the inverse of T_1 and T_2 is shown in **Figure S25**. For T_1, the results can be considered as compliant with the Redfield condition for fields larger than 30 mT, for T_2, the Redfield condition is never met.
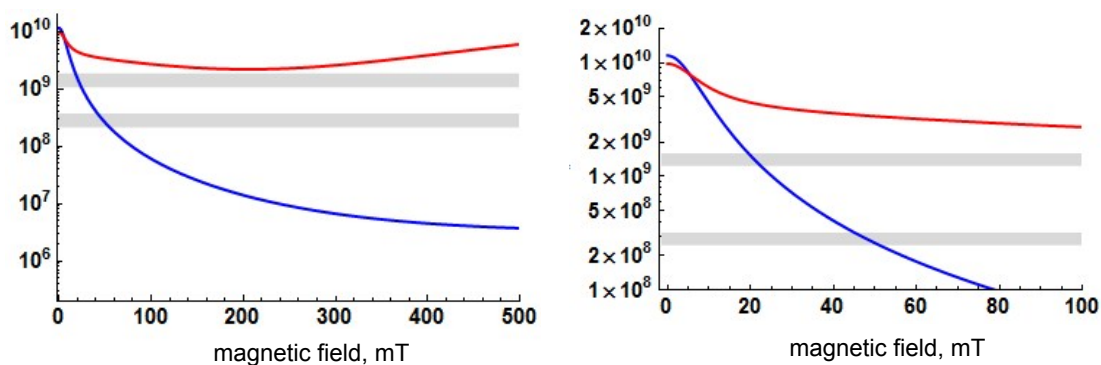

Figure S25 Magnetic field dependence of $1/T_1$ (blue lines) and $1/T_2$ (red lines) as calculated by equations (S10) and (S11) for intermediate (left) and small (right) field scale. Horizontal gray lines correspond to $1/\tau_r$ and $1/5\tau_r$.

On the role of anisotropic hyperfine coupling at low magnetic fields

The processes interconverting the spin substates are induced by a spin Hamiltonian that may be generally decomposed into a time independent part H_0 and a fluctuating part $H'(t)$ with average zero:

$$H(t) = H_0 + H'(t) \tag{S15}$$

The time independent part comprises the effect of isotropic hyperfine coupling and isotropic g-factor difference between the two radicals (Δg-mechanism), and the essential contributions to the time dependent part result from the g-tensor and hyperfine-tensor anisotropies, spin-rotational interaction, and electron spin dipolar interaction. The time independent part gives rise to a coherent spin evolution,

strictly to be described by explicit quantum dynamics. If the correlation times of the fluctuations modulating $H'(t)$ are sufficiently short to fulfil the Redfield condition

$$\tau_c \ll T_1, T_2 \tag{S16}$$

where τ_c is the correlation time of the fluctuation and T_1 and T_2 are the relaxation times obtained by second order time-dependent perturbation theory, the pertinent effects can be reliably described by incoherent relaxation processes with these time constants. The most important source of fluctuating interactions in liquid solution is molecular tumbling, which modulates the effects of g-tensor and hyperfine tensor anisotropies and of electron spin dipolar interaction. Furthermore, it may give rise to spin-rotational coupling. Specific equations for the pertinent relaxation times are available in the literature and have been used to test condition (S16). The correlation times to be considered are the rotational correlation time, τ_R, and the correlation time of angular momentum, τ_ω. These are given by the following expressions:[35]

$$\tau_R = \frac{4\pi\eta}{3kT}R^3 \tag{S17}$$

and
$$\tau_\omega = \frac{\theta}{8\pi\eta R^3} \tag{S18}$$

where η is the solvent viscosity, R the molecular hydrodynamic radius, and θ the molecular moment of inertia. Substituting the specific values of solvent and $^{Me}C^+A_4{}^{8+}$ complex, $\eta = 0.62$ mPa s, $\theta \approx 2.03 \times 10^{-42}$ kg m^2 and $R \approx 10.4$ Å. one can estimate the values $\tau_R \approx 0.71$ ns and $\tau_\omega \approx 0.12$ p s. When the anisotropic hyperfine interaction is modulated, the rotational motion of the complex is too slow to comply with condition (S16). For T_1 at fields below 30 mT and for T_2 at any field, this is a consequence of the strong anisotropy of the Cu hyperfine coupling, and rather exceptional in the field of spin chemistry.[36] It means that, in a correct sense, this anisotropy would have to be taken into account on the time scale of explicit quantum dynamics under conditions of slow molecular tumbling. A full treatment of that kind is beyond the scope of the present work. As an approximation, we will use a modified value of the isotropic hyperfine coupling which will be introduced as an empirical parameter. Since the same type of Lorentzian field dependence as assumed for the coherent mixing process does apply to spin relaxation due to anisotropic

hyperfine coupling (cf. eq (9) in the main text), the Lorentzian approach also includes incoherent contributions in the field regions where condition (S16) does apply. Here coherent and incoherent contributions are indistinguishable. In the case of spin-rotational interaction, which yields a sizeable contribution, condition (S16) is well satisfied by the value of τ_ω.

Moment of inertia

The moment of inertia of $[Cu(^{Me}4OMV)]^{9+}$ was calculated from the geometry shown in **Figure 7** of the main text, using the definition of the elements of the tensor of inertia

$$I_{kl} = I_{lk} = \sum_i m_i \left(r_i^2 \delta_{kl} - x_{ik} x_{il} \right) \tag{S19}$$

where m_i represents the mass of atom i, r_i its radial position, and the x_{ik} its Cartesian coordinates, the indices k and l running over the three dimensions x, y, z. The principle moments of inertia are obtained by diagonalization of this tensor:

$$\theta_{11} = 175462 \, \mathring{A}^2 \times u, \quad \theta_{22} = 166930 \, \mathring{A}^2 \times u, \quad \theta_{33} = 624645 \, \mathring{A}^2 \times u$$

yielding a geometric average of $\theta = 122307 \, \mathring{A}^2 \times u = 2.03.. \times 10^{-42} \, kg \, m^2$.

Estimation of classical rate constants representing coherent mixing processes

S/T$_0$ mixing by Δg-mechanism

For isotropically averaged g-tensors, the Zeeman Hamiltonian of a radical pair is given by

$$H_Z = g_1 \mu_B B_0 S_{1z} + g_2 \mu_B B_0 S_{2z} \tag{S20}$$

It mixes the radical pair state |S> and |T$_0$> by the matrix element

$$\langle S | H_Z | T_0 \rangle = \frac{1}{2} \Delta g \beta B_0 \tag{S21}$$

Then the coherent evolution of singlet probability, when starting from a pure |T$_0$> is given by

$$p_{S,coh}(t) = \frac{1}{2}\left(1 - \cos(\Delta\omega t)\right) \tag{S22}$$

with Δω given by

$$\Delta\omega = \Delta g \beta B_0 \tag{S23}$$

The function $p_S(t)$ is shown in **Figure S26**
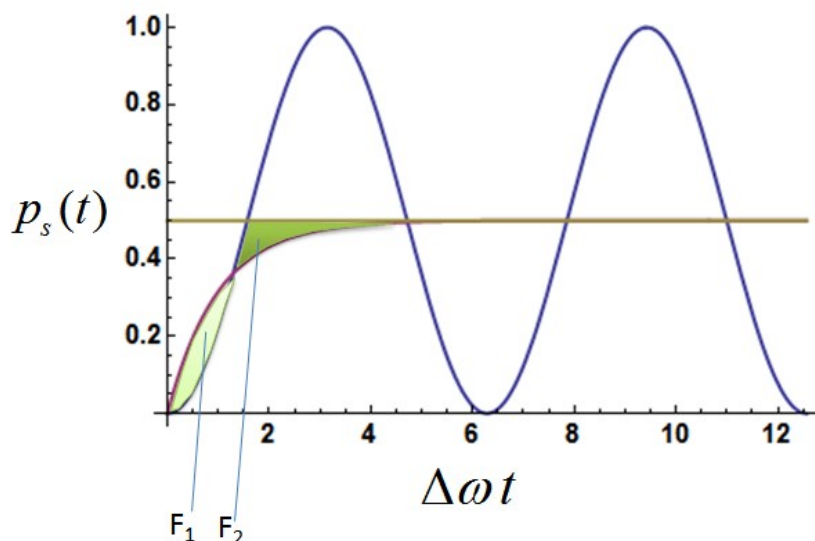
Figure S26 Time dependence of singlet probability for a pure |T$_0$> function at t = 0. Blue: coherent motion according to the Δg-mechanism. Red: exponential approach to equilibrium according to the kinetic model. The rate constant $k_{\Delta g}$ is chosen such as to yield equal areas F$_1$ and F$_2$.

The classical kinetic equilibration between S and T$_0$ is described by the kinetic scheme

$$S \underset{k_{\Delta g}}{\overset{k_{\Delta g}}{\rightleftharpoons}} T_0 \tag{S24}$$

It leads to the following kinetics of equilibration:

$$p_{S,kin} = \frac{1}{2}\left(1 - \exp\left[-2k_{\Delta g}t\right]\right)$$ (S25)

For matching the classical with the quantum kinetics, one may assume that the time integrals over

$p_{S,coh} - p_{S,kin}$ before the crossing point of both curves and $Min\left[p_{S,coh}, \frac{1}{2}\right] - p_{S,kin}$ after the crossing

point for $\Delta\omega t < 3\pi/2$ plus the time integral over $\frac{1}{2} - p_{S,kin}$ for t ≥ 3π/2 (cf. shaded areas in **Figure S26**)

are equal. This leads to the equation

$$k_{\Delta g} = \frac{1}{2}\Delta\omega$$ (S26)

General S/T$_0$ mixing and S/T$_\pm$ and T$_0$/T$_\pm$ mixing in zero field by isotropic hfc

If we assume the following classical kinetic schemes for zero field

$$S \underset{k_{hfc}}{\overset{k_{hfc}}{\rightleftharpoons}} T_0 \,,$$

$$S \underset{k_{hfc}}{\overset{k_{hfc}}{\rightleftharpoons}} T_\pm$$ (S27)

$$T_0 \underset{k_{hfc}}{\overset{k_{hfc}}{\rightleftharpoons}} T_\pm$$

and high field

$$S \underset{k_{hfc}}{\overset{k_{hfc}}{\rightleftharpoons}} T_0 \,,$$ (S28)

and we start with an equal population of the triplet states, the evolution of the singlet population is as

follows. At zero field

$$p_{S,zF}(t) = \frac{1}{4}\left(1 - \exp\left[-4k_{hfc,0}t\right]\right)$$ (S29)

and at high field

$$p_{S,hF}(t) = \frac{1}{6}\left(1 - \exp\left[-2k_{hfc,0}t\right]\right)$$ (S30)

We will compare the resulting behavior with the semiclassical spin motion for zero field and high field as

derived by Schulten and Wolynes[37] According to these authors the isotropic hyperfine coupling situation

in each radical is reduced to a characteristic time constant τ_I by the relation

$$\frac{1}{\tau_i^2} = \frac{1}{6}\sum a_{ik}^2 I_{ik}(I_{ik}+1) \qquad \text{(S31)}$$

In zero field the singlet probability of an initial triplet radical pair is given by

$$p_{S,zF} = \frac{1}{4}\left\{1 - \frac{1}{9}[1+2f(t/\tau_1)][1+2f(t/\tau_2)]\right\} \qquad \text{(S32)}$$

with the definition

$$f(x) = (1-2x^2)\exp(-x^2) \qquad \text{(S33)}$$

In high field, the result is

$$p_{S,hF}(t) = \frac{1}{6}\left[1 - \exp\left(-t^2/\tau_1^2\right)\exp\left(-t^2/\tau_2^2\right)\right] \qquad \text{(S34)}$$

In eq (S35) the two individual time constants can be contracted to a single one by using the definition

$$\frac{1}{\tau^2} = \frac{1}{\tau_1^2} + \frac{1}{\tau_2^2} \qquad \text{(S35)}$$

With this definition, eq (S35) is simplified to

$$p_{S,hF}(t) = \frac{1}{6}\left[1 - \exp\left(-t^2/\tau^2\right)\right] \qquad \text{(S36)}$$

It may be of interest to relate the characteristic time constants τ_1, τ_2, and τ to the characteristic fields B_1, B_2, and $B_{1/2}$ used in the spin chemical literature.[38] The relations are:

$$B_i = \left(\sum a_{ik}^2 I_{ik}(I_{ik}+1)\right)^{1/2} kl \qquad \text{(S37)}$$

Hence

$$\tau_i = \frac{\sqrt{6}}{B_i} kl \qquad \text{(S38)}$$

The simplest relation between B_1, B_2, and $B_{1/2}$ is[39]

$$B_{1/2}^2 = 3(B_1^2 + B_2^2) kl \qquad \text{(S39)}$$

Hence

S42

$$\tau \approx \frac{3\sqrt{2}}{B_{1/2}} \tag{S40}$$

In **Figure S27** the various functions of $p_S(t)$ are shown for the specific example of the $Cu(^{Me}phen)_2{}^+..MV^{2+}$ radical pair. If one chooses $k_{hfc,0}$ in the classical kinetics description by the criterion that for the high-field curve the integrals over classical and semiclassical curves should be equal, one can derive the relation

$$k_{hfc,0} = \frac{1}{\sqrt{\pi}\,\tau} = \frac{B_{1/2}}{3\sqrt{2\pi}} \tag{S41}$$

which does not depend on the individual values τ_i or B_i of the two radicals.
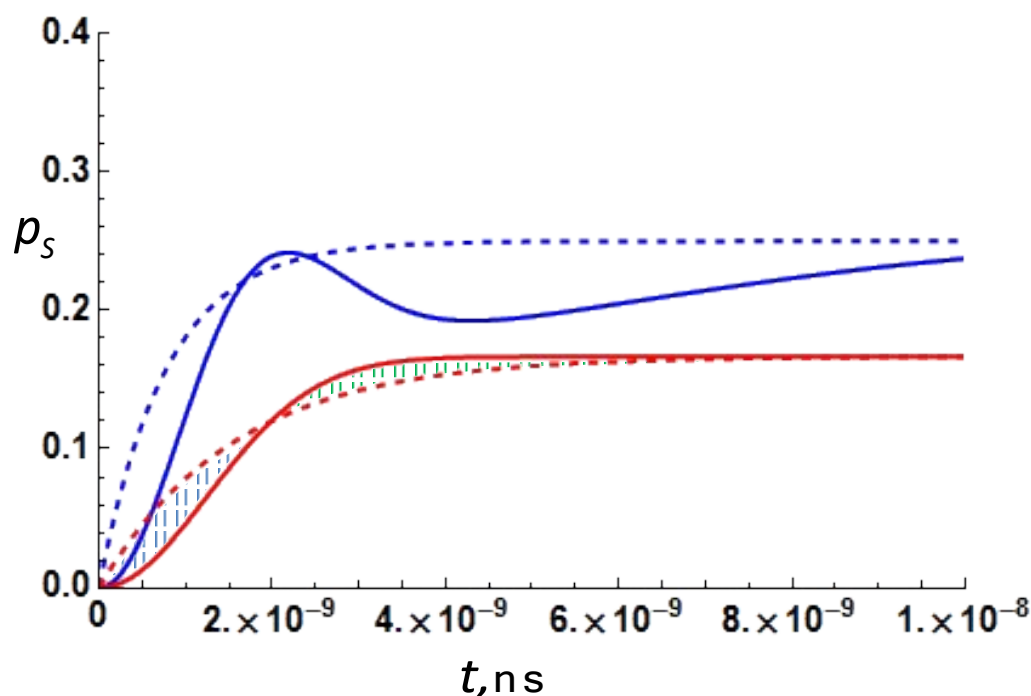
Figure S27 Spin motion due to isotropic hyperfine coupling. Solid curves: semi-classical model for radical pair $(Cu(^{Me}phen)_2{}^+..MV^{2+}$ B_1 = 78 G , B_2 = 12.5 G, $B_{1/2}$ = 137 G). Blue: zero field, red: high field. Dashed curves: classical kinetics (eqs. (S29) and S(39)). The rate constant $k_{hfc,0}$ = 3.2×10^8 s^{-1} was chosen such that the two shaded areas between the classical and the semi-classical high field curves became equal.

Advanced semiclassical theory

The semiclassical approach to hyperfine controlled spin motion in radical pairs by Schulten and coworkers[37,40] has recently been extended by Lewis, Manolopoulos and Hore.[41,42] In these advanced versions, each nuclear spin vector is allowed to precess independently around the electron spin vector

whereas in the original versions a hyperfine weighted sum of nuclear spins was used. Furthermore, the method has been extended to account for different reactivity of singlet and triplet.

The authors of ref. 42 kindly provided us with a program code to apply the extended semiclassical theory to our system.

The following hyperfine constants have been used: Cu: I = 3/2, a = -4,0 mT, MV$^+$: $4 \times a_H$= 0.134 mT, $4 \times a_H$= 0.159 mT, $6 \times a_H$= 0.401 mT.

First, we calculated the hyperfine induced spin motion without reaction (cf. **Figure S28** to compare it with the result obtained by the Schulten method.
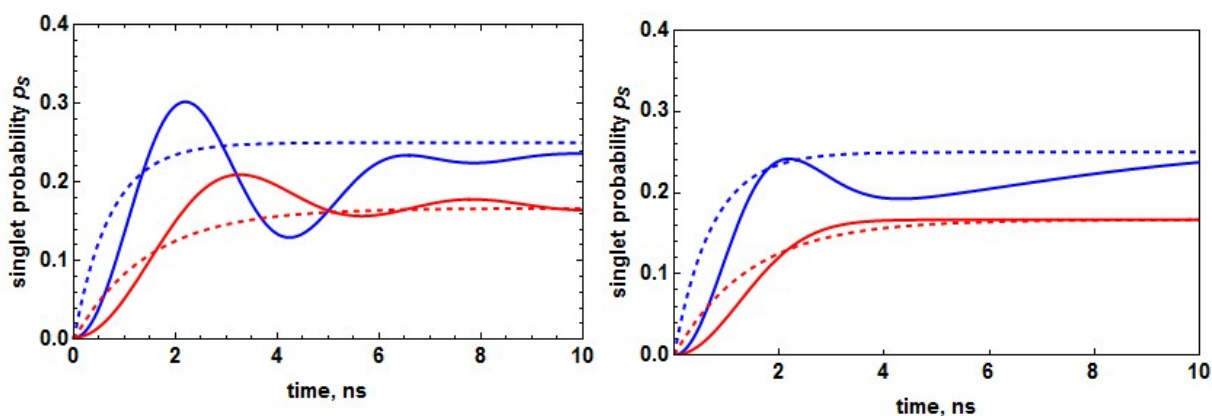
Figure S28 Semiclassical spin motion, evolution of singlet character in a Cu(II)/MV$^+$ radical pair, when starting in a pure triplet. Blue: zero field, red. High field limit. The dashed lines correspond to classical kinetics with k_{TS0} = 3.8 x 10^8 s^{-1}.Left: Coherent spin motion according to Lewis et al.[42] right: according to Schulten and Wolynes.[37] Both diagrams show the same classical kinetics curves.

In the more advanced calculations, the spin motion shows stronger oscillations, but the purely exponential substitutes we used in our classical kinetics model fits the more advance model even better.

For the full treatment, including reaction, a field dependent parametrization of spin relaxation times must be provided for the advanced semiclassical model. To this end, we took the spin relaxation times following from our treatment. The field dependent values of the relaxation times (only the Cu(II) complex was considered) were obtained by the following equations, based on eqs. (2), (7) and (8) in the main paper:

$$\frac{1}{T_2'} = 2(k_{TS0}[B] - k_{hfc0}) \tag{S42}$$

$$\frac{1}{T_1} = 4(k_1[B] - k_{hfc}[B]) \qquad (S43)$$

$$\frac{1}{T_2} = \frac{1}{T_2'} + \frac{1}{2T_1} \qquad (S44)$$

Thus, we made sure that the classical treatment in our paper and the advanced semiclassical treatment differed only in the way the effect of hyperfine coupling was dealt with, while employing the same contributions of spin relaxation.

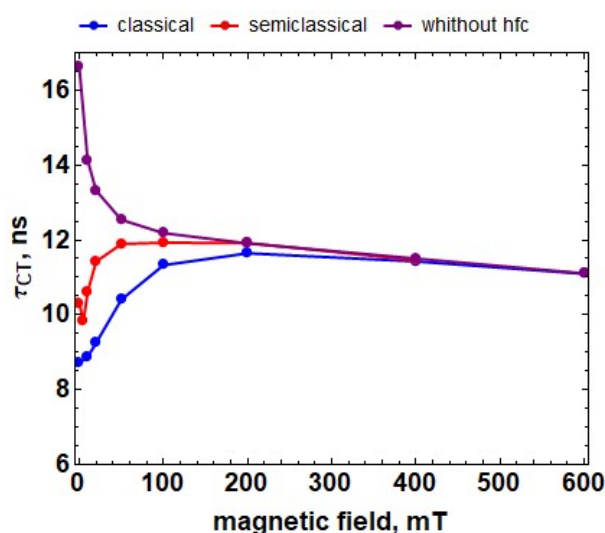The Δg effect was implicitly taken into account through the value of relaxation time T_2' of the Cu(II) complex.

Figure S29 Calculated CT recombination lifetime using the classical model (blue, fitting the experimental data), the advanced semiclassical model with hyperfine interaction and relaxation (red) and classical and semiclassical model with relaxation only (violet).

As it appears from the results shown in **Figure S29**, coherent hyperfine driven spin motion as treated by the advanced semiclassical method is not sufficient to account for recombination at field below ca. 200 mT. Here anisotropic hyperfine contributions under conditions of slow rotational motion as implicitly included in the empirical equation, eq. (8), of the classical model, must be invoked. At fields above ca. 200 mT spin relaxation is sufficient to account for the recombination lifetime.

As can be seen in **Figure S29**, a low-field effect (shortening of lifetime with increasing field, minimum at about 5 mT) appears as a result of purely coherent spin motion. Such an effect does not appear in the experiment, or may escape detection, due to scatter of experimental data. Anyway, we would not expect

S45

it to occur if anisotropic hyperfine interactions under rotational slow-motion conditions did contribute to spin evolution.
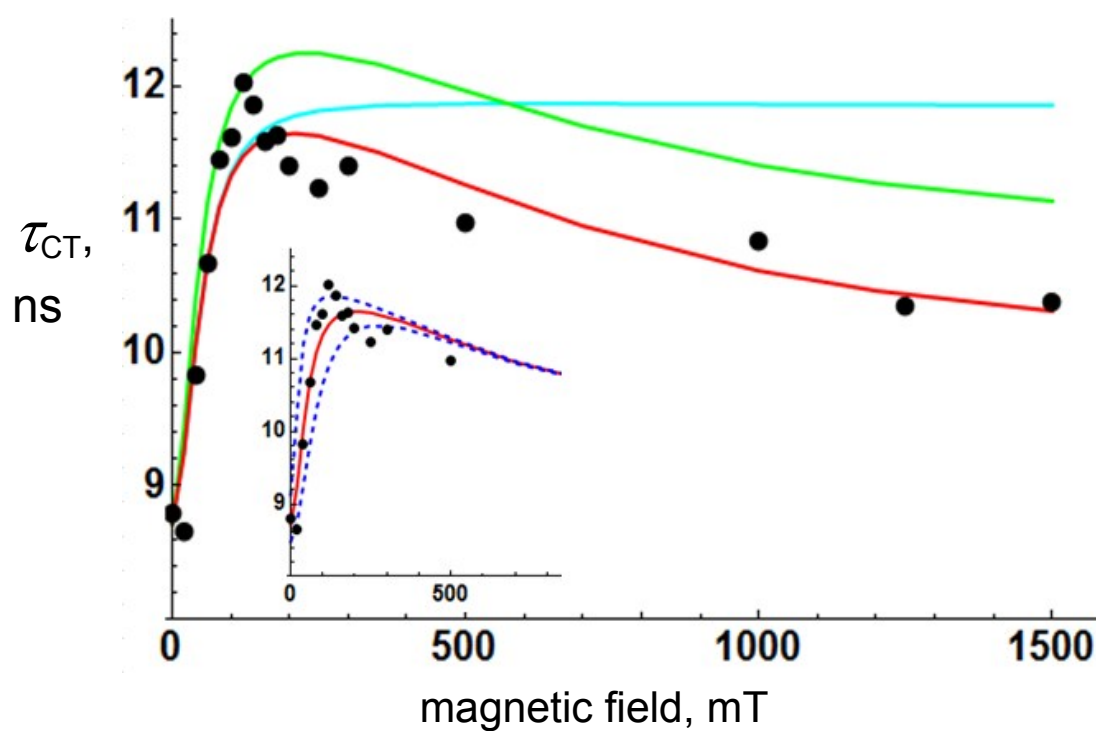
Supplementary Diagrams

Figure S30 Fitting τ_{CT} for $^{Ph}C^+A_4^{8+}$. Black: data points, red line: best fit, using the parameters given in **Table 1** from the main text, green line: without the effect of Δg-mixing, blue line: without the effect of internal gta-mechanism. Inset: lower dashed line: for $B_{hfc,1/2}$ = 20 mT, upper dashed line: for $B_{hfc,1/2}$ = 10 mT
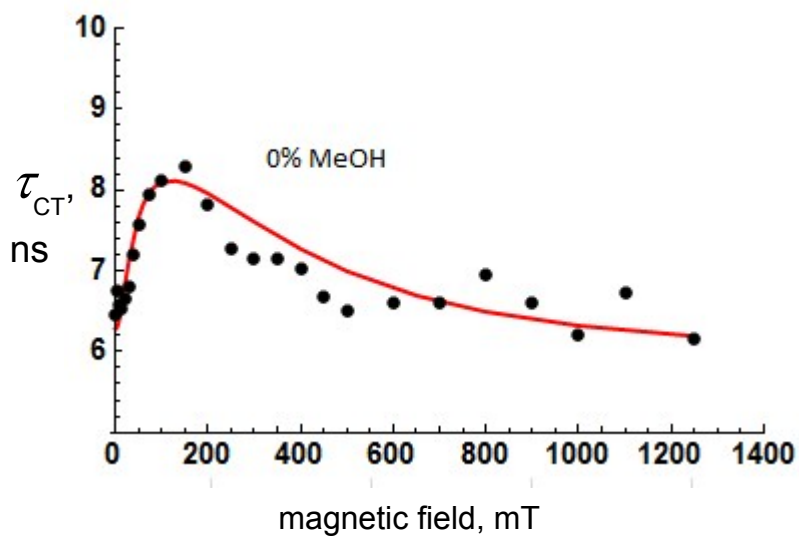
Figure S31 Data points: lifetime of charge separated state for $^{Me}C^+A_4^{8+}$ in dfb. Red curve: simulation using the parameters given in **Table 1** of the main text.
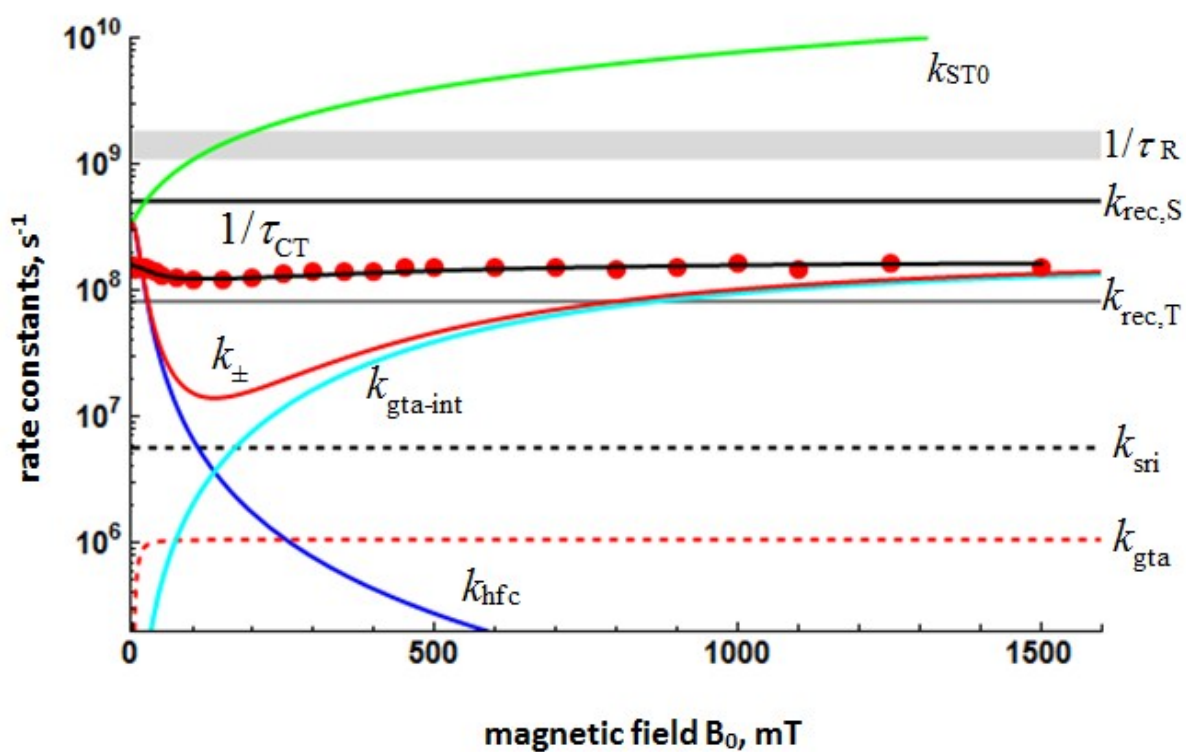
Figure S32 Magnetic field dependence of various contributions to spin dynamics and related parameters for $^{Me}C^+A_4^{8+}$ in pure dfb. Red data points: inverse of experimental τ_{CT} values with best fit line from **Figure S31** in black.
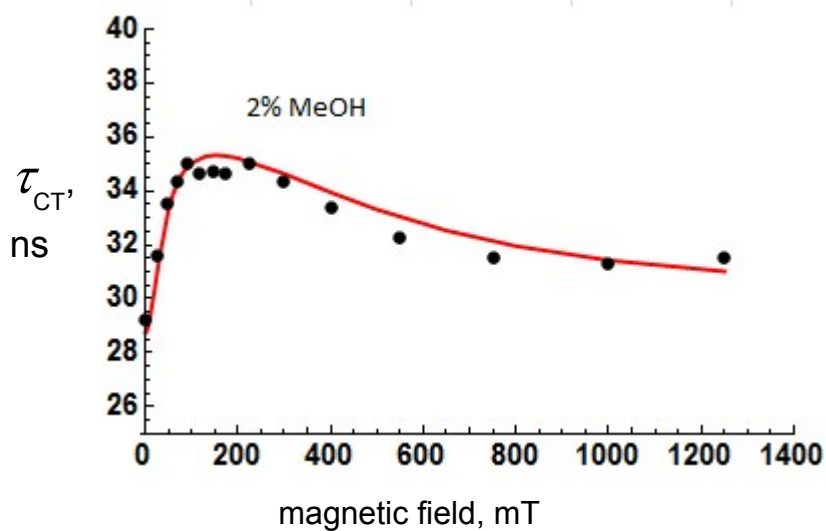
Figure S33 Data points: lifetime of charge separated state for $^{Me}C^+A_4^{8+}$ in dfb/2% MeOH. Red curve: simulation using the parameters given in **Table 1** of the main text.
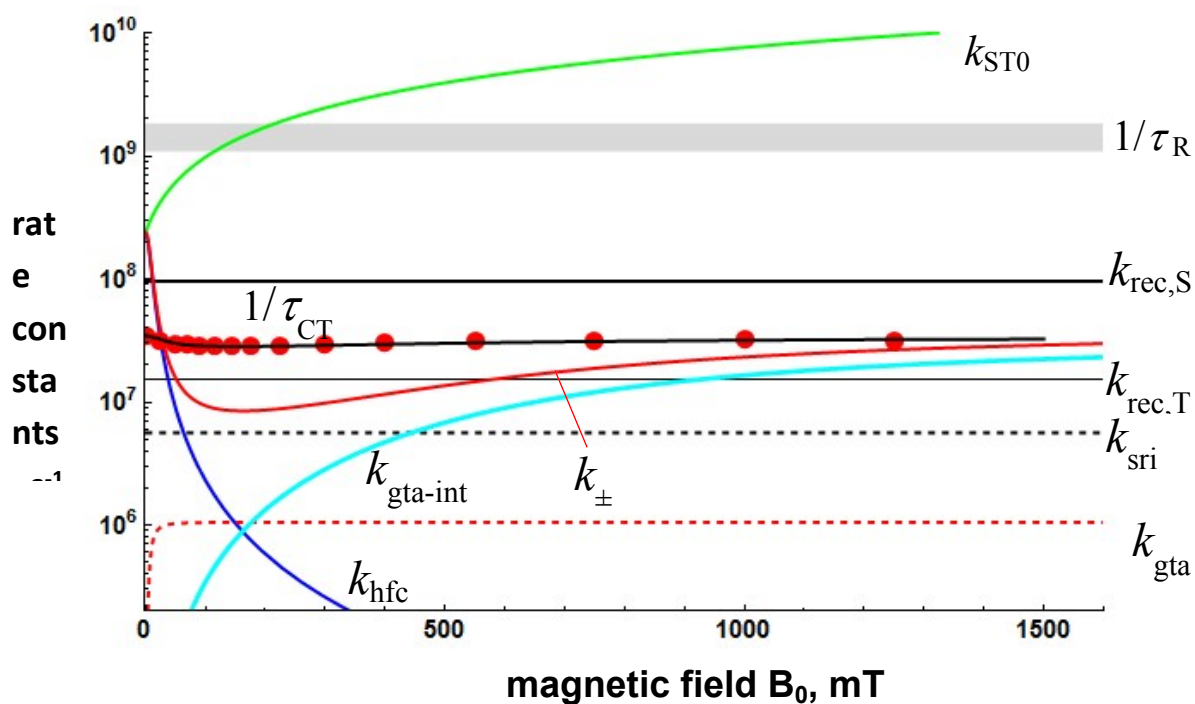

Figure S34 Magnetic field dependence of various contributions to spin dynamics and related parameters for $^{Me}C^+A_4^{8+}$ in dfb/2% MeOH. Red data points: inverse of experimental τ_{CT} values with best fit line from **Figure S33** in black.
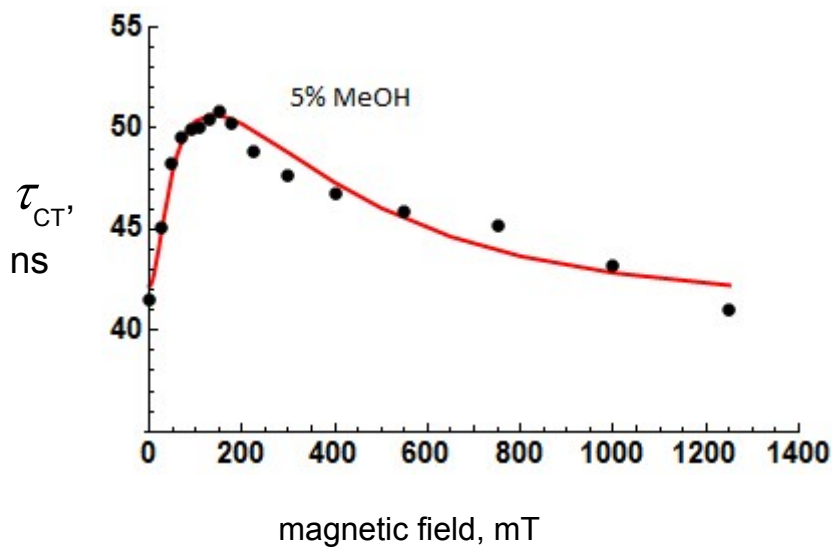
Figure S35 Data points: lifetime of charge separated state for $^{Me}C^+A_4^{8+}$ in dfb/5% MeOH. Red curve: simulation using the parameters given in **Table 1** of the main text.

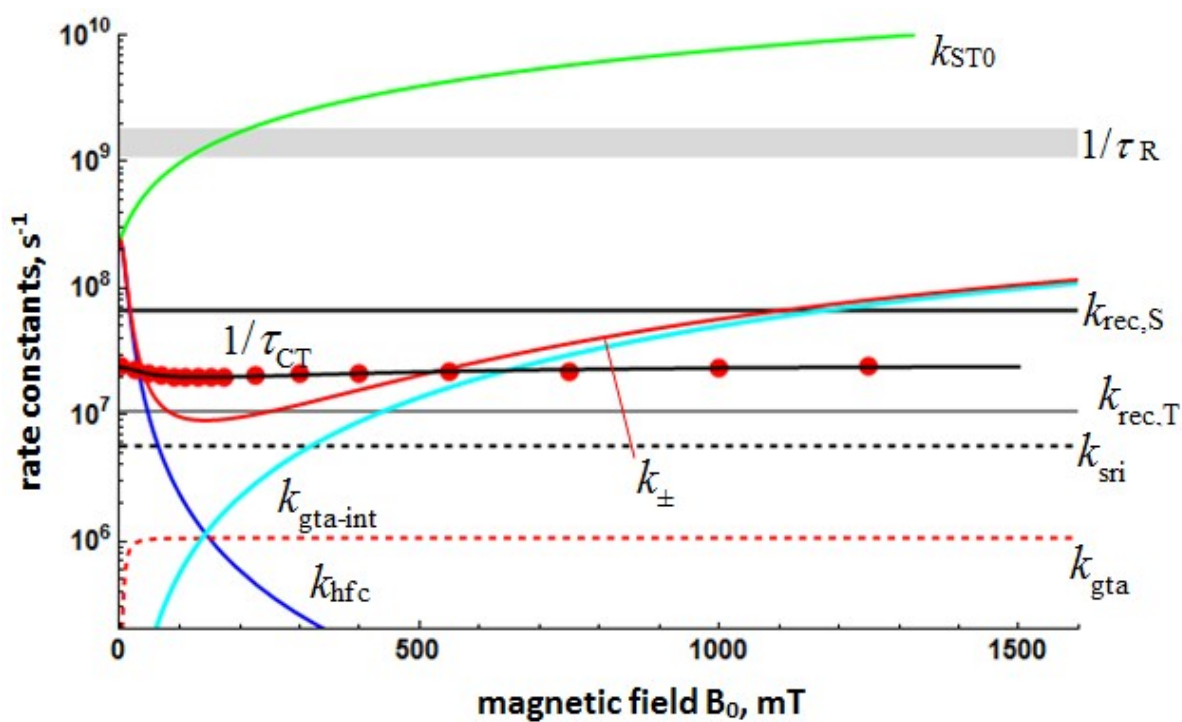**Figure S36** Magnetic field dependence of various contributions to spin dynamics and related parameters for $^{Me}C^+A_4^{8+}$ in dfb/5% MeOH. Red data points: inverse of experimental τ_{CT} values with best fit line from **Figure S35** in black.
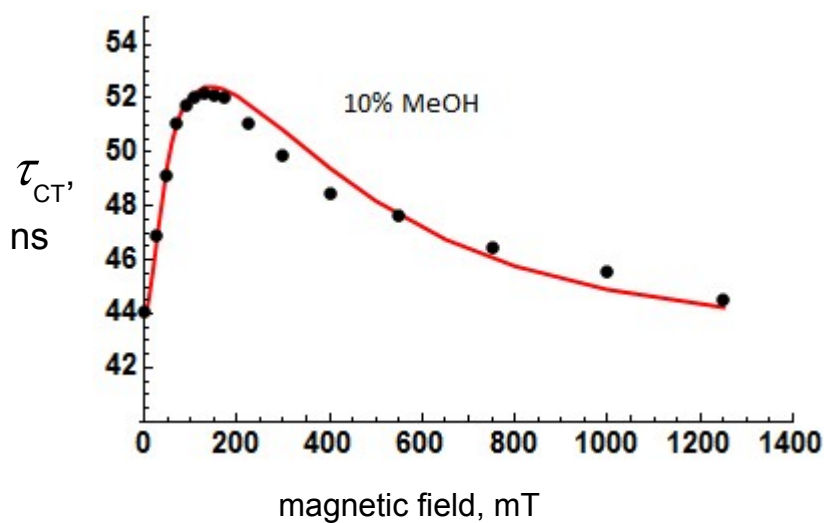
Figure S37 Data points: lifetime of charge separated state for $^{Me}C^+A_4^{8+}$ in dfb/10% MeOH. Red curve: simulation using the parameters given in **Table 1** of the main text.

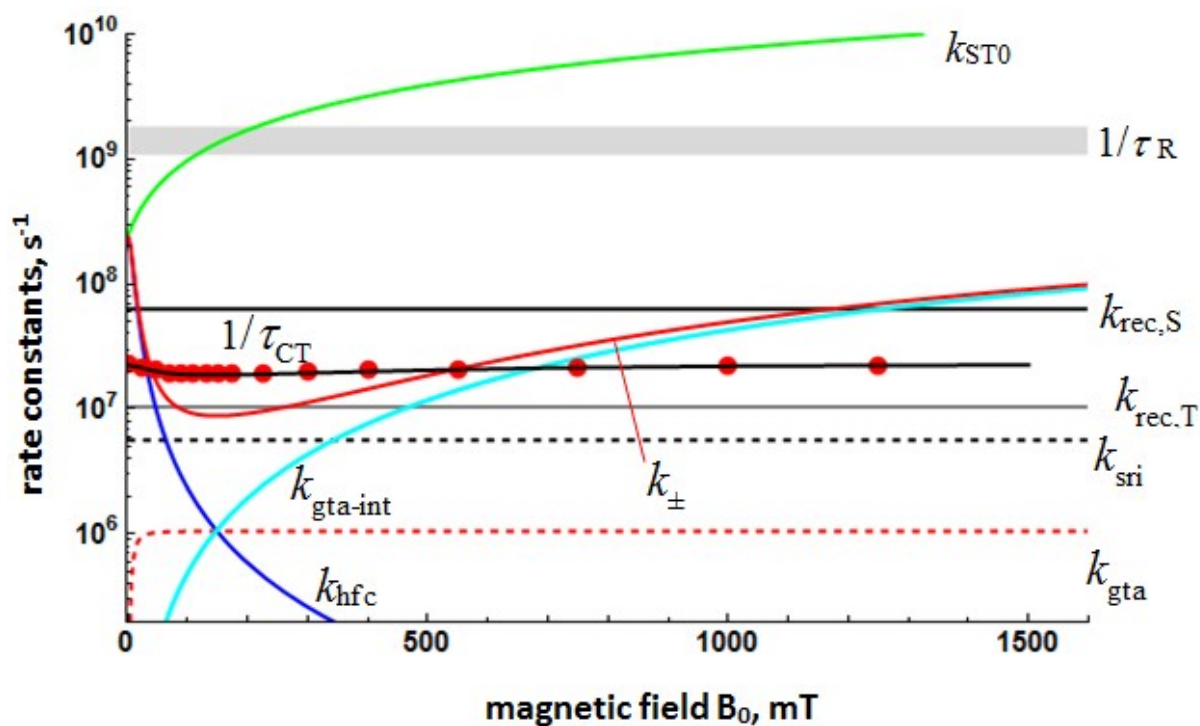**Figure S38** Magnetic field dependence of various contributions to spin dynamics and related parameters for $^{Me}C^+A_4^{8+}$ in dfb/10% MeOH. Red data points: inverse of experimental τ_{CT} values with best fit line from **Figure S37** in black.

I. References

1. J. Hong, M. P. Shores and C. M. Elliott, *Inorg. Chem.*, 2010, **49**, 11378–11385.

2. F. Calderazzo, F. Marchetti, G. Pampaloni and V. Passarelli, *J. Chem. Soc. Dalt. Trans.*, 1999, 4389–4396.

3. A. M. S. Garas and R. S. Vagg, *J. Heterocycl. Chem.*, 2000, **37**, 151–158.

4. N. Margiotta, V. Bertolasi, F. Capitella, L. Maresca, A. G. G. Moliterni, F. Vizza and G. Natile, *Inorganica Chim. Acta*, 2004, **357**, 149–158.

5. A. P. Lehnig, M. S. Lazorski, M. Mingroni, K. A. O. Pacheco and C. Michael Elliott, *J. Heterocycl. Chem.*, 2014, **51**, 1468–1471.

6. J.-Z. Wu, H. Li, J.-G. Zhang and J.-H. Xu, *Inorg. Chem. Commun.*, 2002, **5**, 71–75.

7. M. L. Rizzo, *Statistical Computing with R*, CRC Press, Boca Raton, 2007.

8. T. Petrenko, S. Kossmann and F. Neese, *J. Chem. Phys.*, 2011, **134**, 054116.

9. G. B. Shaw, C. D. Grant, H. Shirota, E. W. C. Jr, G. J. Meyer and L. X. Chen, *J. Am. Chem. Soc.*, 2007, **129**, 2147–2160.

10. D. V Scaltrito, D. W. Thompson, J. a O'Callaghan and G. J. Meyer, *Coord. Chem. Rev.*, 2000, **208**, 243–266.

11. A. K. Ichinaga, J. R. Kirchhoff, D. R. McMillin, C. O. Dietrich-Buchecker, P. A. Marnot and J. P. Sauvage, *Inorg. Chem.*, 1987, **26**, 4290–4292.

12. M. Iwamura, S. Takeuchi and T. Tahara, *J. Am. Chem. Soc.*, 2007, **129**, 5248–5256.

13. G. J. Atchity, S. S. Xantheas and K. Ruedenberg, *J. Chem. Phys.*, 1991, **95**, 1862–1876.

14. T. J. Martinez, *Nature*, 2010, **467**, 412–413.

15. F. Neese, *J. Phys. Chem. Solids*, 2004, **65**, 781–785.

16. M. Iwamura, S. Takeuchi and T. Tahara, *Phys. Chem. Chem. Phys.*, 2014, **16**, 4143–4155.

17. F. Neese, *J. Chem. Phys.*, 2001, **115**, 11080.

18. F. Neese, *J. Chem. Phys.*, 2003, **118**, 3939.

19. B. Sandhoefer and F. Neese, *J. Chem. Phys.*, 2012, **137**, 094102.

20. B. Sandhoefer, S. Kossmann and F. Neese, *J. Chem. Phys.*, 2013, **138**, 104102.

21. L. Visscher and K. G. Dyall, *At. Data Nucl. Data Tables*, 1997, **67**, 207–224.

22. F. Neese, *Inorganica Chim. Acta*, 2002, **337**, 181–192.

23. S. Sinnecker and F. Neese, *J. Comput. Chem.*, 2006, **27**, 1463–75.

24. K. M. Lancaster, M.-E. Zaballa, S. Sproules, M. Sundararajan, S. DeBeer, J. H. Richards, A. J. Vila, F. Neese and H. B. Gray, *J. Am. Chem. Soc.*, 2012, **134**, 8241–53.

25. S. Vancoillie, P.-A. Malmqvist and K. Pierloot, *Chemphyschem*, 2007, **8**, 1803–15.

26. F. Neese, *Magn. Reson. Chem.*, 2004, **42 Spec no**, S187-98.

27. M. T. Miller, P. K. Gantzel and T. B. Karpishin, *Inorg. Chem.*, 1998, **37**, 2285–2290.

28. F. Neese, *J. Phys. Chem. A*, 2001, **105**, 4290–4299.

29. J. R. Kirchhoff, R. E. Gamache, M. W. Blaskie, A. A. D. Paggio, R. K. Lengel and D. R. McMillin, *Inorg. Chem.*, 1983, **22**, 2380–2384.

30. Z. A. Siddique, Y. Yamamoto, T. Ohno and K. Nozaki, *Inorg. Chem.*, 2003, **42**, 6366–78.

31   M. Iwamura, H. Watanabe, K. Ishii, S. Takeuchi and T. Tahara, *J. Am. Chem. Soc.*, 2011, **133**, 7728–7736.

32   S. Garakyaraghi, E. O. Danilov, C. E. McCusker and F. N. Castellano, *J. Phys. Chem. A*, 2015, **119**, 3181–3193.

33   L. Banci, I. Bertini and C. (Claudio) Luchinat, *Nuclear and electron relaxation*, VCH Publishers Inc., New York, 1991.

34   J. H. Klein, D. Schmidt, U. E. Steiner and C. Lambert, *J. Am. Chem. Soc.*, 2015, **137**, 11011–11021.

35   P. W. Atkins and D. Kivelson, *J. Chem. Phys.*, 1966, **44**, 169.

36   Note: In $[Ru(bpy)_3]^{3+}$ the *g*-tensor anisotropy is quite high, but in radical pairs involving that species the dominating spin conversion mechanism is spin relaxation by the rotation-independent Orbach mechanism (cf. K. A. Hötzer, A. Klingert, T. Klumpp, E. Krissinel, D. Bürßner, and U. E. Steiner, *J. Phys. Chem. A.*, 2002, **106**, 2207-2217).

37   K. Schulten and P. G. Wolynes, *J. Chem. Phys.*, 1978, **68**, 3292.

38   A. Weller, F. Nolting and H. Staerk, *Chem. Phys. Lett.*, 1983, **96**, 24–27.

39   U. E. Steiner and H. J. Wolff, in *Photochemistry and Photophysics*, eds. J. J. Rabek and G. W. Scott, CRC Press, Boca Raton, 1991, vol. IV, pp. 1–130.

40   E.-W. Knapp and K. Schulten, *J. Chem. Phys.*, 1979, **71**, 1878.

41   D. E. Manolopoulos and P. J. Hore, *J. Chem. Phys.*, 2013, **139**, 124106 (1–8).

42   A. M. Lewis, D. E. Manolopoulos and P. J. Hore, *J. Chem. Phys.*, 2014, **141**, 44111.